Fig. 1. Geological zonings and locations of borehole explorations in the urban area of Suzhou.

structure at this site can be characterized with linear interpolation or Kriging-based interpolation methods (Patel and McMechan, 2003; Hu, 2006). In consideration of the uncertainties involved in this site characterization, the geotechnical parameters at the concerned site could be characterized with a random field (Wang et al., 2010; Cao and Wang, 2012; Gong et al., 2014, 2016) or a conditional random field (Li et al., 2015, 2016b; Wang and Zhao, 2017); and, the stratigraphic structure at this site could be characterized using a Markov chain (Hu and Huang, 2007; Li et al., 2016c; Qi et al., 2016).

Though theoretically sound, the probabilistic methods (e.g., random field, conditional random field and Markov chain) are generally computationally prohibitive, which could only be practically applicable to critical projects. It is worth noting that the site characterization is, indeed, a three-dimensional (3D) problem and the site information could vary spatially along both horizontal and vertical directions. Here, this 3D feature would further complicate the site characterization (from the site information available at borehole locations). As a matter of fact, most discussions on the site characterization, outlined in the aforementioned literature, only deal with the characterization of the site information in a given cross-section or that at a given depth at the concerned site. That is to say, the site characterization, in the current practice, is oftentimes approximated as a two-dimensional (2D) problem.

In the context of a 3D site characterization, the concerned site is first discretized into a set of smaller zones, and then the geotechnical and geological information within each smaller element is characterized from the site information available at borehole locations. This 3D site characterization can be conducted utilizing either surface-based methods (Pishbin et al., 2016; Wang et al., 2017) or solid-based methods (Lemon and Jones, 2003; Houlding, 2012). Within the surface-based methods, the site information at the surfaces of the discretized zones can be derived while that within the corresponding zones cannot be derived. Thus, the surface-based methods are especially suitable for characterizing the ground surfaces, faults and interfaces between strata; whereas, the solid-based methods could be more capable of characterizing the site information within the discretized zones, and certainly the solid-based methods demand substantially more computational effort. It is noted that another significant issue in the 3D site characterization is the visualization of the characterized site information. The characterized site information could be mapped to AutoCAD (Sitharam et al., 2007) or ArcGIS Engine (Lan et al., 2009; Kumar, 2012). In that

the size of the borehole data, which could be afforded in the existing site characterizations, is usually small owing to the very limited budget for the site investigation, neither 3D characterization nor 3D visualization of the site information has been extensively reported in literature. Further, the limited availability of the borehole data would degrade the effectiveness of the 3D site characterization and 3D site visualization.

In such a circumstance, this paper presents a 3D site characterization in Suzhou, China where plenty of borehole data have been collected. With the collected borehole data, the data on the shear-wave velocity are studied to illustrate the spatial variation of the geotechnical parameters along the depth, then a sequence extrapolation method that is capable of predicting the shear-wave velocity along the depth is developed. Next, the data regarding the sequence stratigraphic structures available at borehole locations are studied, and then the Kriging-based interpolation method is used to characterize the 3D stratigraphic model in Suzhou. With the aid of ArcGIS Engine, a 3D visualization of the resulting 3D stratigraphic model is realized. The rest of this paper is organized as follows. First, a borehole database which consists of the borehole data in the urban area of Suzhou is established. Second, a spatial characterization of the shear-wave velocity along the depth, in the urban area of Suzhou, is presented. Third, a 3D characterization and visualization of the stratigraphic model, in the urban area of Suzhou, are presented. Finally, the concluding remarks are drawn based upon the results presented.

2. Borehole database establishment: borehole data in urban area of Suzhou

Suzhou is a major city located in the southeast of Jiangsu Province, China, about 50 km northwest to Shanghai. The history of Suzhou could be traced back to about 500 BC and it is well known for its canals, stone bridges, pagodas and classical gardens. This city is situated on the lower reaches of Yangtze River and the shores of Lake Tai, and belongs to the Yangtze River Delta region. The focus of this paper is on the spatial characterization of the shear-wave velocity and the 3D characterization and visualization of the stratigraphic model in the urban area of Suzhou where plenty of borehole explorations have been undertaken. The engineering geology and the borehole database establishment in the urban area of Suzhou are summarized below.

Table 1

A short description of the sources of 397 sets of borehole data studied in this paper.[a]

Source of boreholes	No.	Relative coordinates[b] (X, Y) (m)	Borehole depth (m)	Source of boreholes	No.	Relative coordinates[b] (X, Y) (m)	Borehole depth (m)
Technology Building 3-10th Blocks in Suzhou National Hi-Tech District	J1	(− 17,168.9, 1577.6)	85	Suzhou Communication Logistics Operations Center	J33	(− 7879.6, 4589.0)	100
	J2	(− 17,141.4, 1584.2)	87		J34	(− 7995.2, 4685.6)	100
	J3	(− 17,160.5, 1485.4)	84		J35	(− 8271.9, 4690.0)	100
Gas Turbine Cogeneration Project in the North of Suzhou Industrial Park	J4	(3913.0, 1654.1)	101	Suzhou Green Peak South Gate Green County Community	J36	(184.0, − 3371.9)	100
	J5	(3895.0, 1676.3)	100		J37	(263.7, − 3464.1)	99
Suzhou General Hospital	J6	(− 20,188.0, 3933.0)	100	Suzhou Platinum Hanjue Hotel	J38	(2576.6, − 7912.9)	98
	J7	(− 20,193.8, 3898.4)	100		J39	(2595.5, − 7904.1)	100
North Ring Expressway-auxiliary Tunnel	J8	(− 745.2, 1477.7)	100	Suzhou Wuzhong Business Center	J40	(− 2321.0, − 11,067.6)	97
	J9	(− 890.3, 1443.2)	100		J41	(− 2404.5, − 11,094.2)	102
	J10	(− 958.6, 1425.5)	100		J42	(− 2468.1, − 11,139.7)	101
Suzhou Public Security Command Center	J11	(− 733.5, 4040.6)	99	Suzhou Dongdu International Building	J43	(− 7054.0, − 948.8)	14
	J12	(− 732.7, 4051.7)	100		J44	(− 7054.0, − 948.8)	20
International Business Square in Suzhou National Hi-Tech District	J13	(− 4832.4, − 2033.3)	118	Suzhou Avic Hotel	J45	(− 18,832.1, 3626.6)	83
	J14	(− 4817.3, − 2053.3)	130		J46	(− 18,713.5, 3662.1)	85
East Extension Section of Suzhou Rail Transit Line 1	J15	(− 1701.9, 1357.8)	100	No. 2010-B-41 Block of Suzhou	J47	(− 7467.3, 5960.9)	100
	J16	(11,800.0, 1246.8)	98		J48	(− 7242.6, 6047.5)	100
	J17	(10,719.2, 1113.6)	99		J49	(− 7512.8, 5908.8)	97
	J18	(9448.8, 1009.2)	97		J50	(− 7388.6, 5888.8)	98
	J19	(8709.3, 919.3)	100		J51	(− 7218.0, 5918.8)	98
	J20	(8007.5, 1014.8)	100		J52	(− 7287.3, 5838.8)	100
Xingtang Street Interchange	J21	(11,231.5, 3527.8)	100	No. 2003-B-42 Suzhou Sudi Block	J53	(− 4196.9, − 1851.2)	100
	J22	(11,633.4, 3593.3)	100		J54	(− 4138.1, − 1932.3)	100
Suzhou Zhongrun Square	J23	(1126.2, − 5359.9)	100	Suzhou Rail Transit Line 1 Control Center	J55	(− 1854.1, − 1082.0)	95
	J24	(1211.6, − 5431.0)	100		J56	(− 1951.8, − 1102.0)	100
Comprehensive Renovation Project of Suzhou Wuzhong People's Hospital	J25	(633.8, − 5032.5)	100	Culture and Arts Centre in Suzhou National Hi-Tech District	J57	(− 17,334.8, 2747.5)	95
	J26	(722.0, − 5031.4)	90		J58	(− 17,211.6, 2753.0)	93
Suzhou Taiping Financial Building	J27	(9359.6, 1057.0)	100	Suzhou Pingjiang Comprehensive Convenience Service Center	J59	(− 855.1, 3207.0)	100
	J28	(9377.6, 1031.4)	100		J60	(− 1023.8, 3201.5)	100
	J29	(9442.1, 1015.9)	100		J61	(− 918.6, 3228.1)	100
	J30	(9421.2, 1085.8)	100		J62	(− 1021.0, 3212.6)	100
Relocation of Suzhou Hospital of Traditional Chinese Medicine	J31	(− 2238.1, − 5102.4)	100	Comprehensive Housing of Suzhou Power Supply Company	J63	(− 1702.5, − 2280.8)	100
	J32	(− 2064.8, − 4989.2)	97				
Yangcheng Lake Bridge	J64	(17,383.4, 6610.3)	100	Suzhou Science and Technology Town	J102	(− 17,495.7, 1797.3)	70
	J65	(18,509.2, 6649.1)	99		J103	(− 17,350.7, 1717.4)	70
	J66	(19,677.8, 7099.8)	100		J104	(− 17,290.1, 1696.3)	71
Technology Incubator in Suzhou Technology City	J67	(− 18,707.6, 2703.1)	54	Wu Songjiang Bridge in Suzhou Industrial Park	J105	(16,189.1, − 1796.8)	100
	J68	(− 18,740.9, 2660.9)	31		J106	(16,189.5, − 2058.8)	94
	J69	(− 18,689.7, 2644.3)	51		J107	(16,183.2, − 2294.1)	95
Suzhou Nisheng Square	J70	(4338.4, 30.2)	98	Suzhou Shishan Square	J108	(− 6664.0, − 2097.7)	100
	J71	(4260.7, − 67.5)	90		J109	(− 6656.4, − 2102.1)	95
People's Road in Suzhou Sulun Square	J72	(84.4, − 3163.3)	101	No. 2010-G-18 Suzhou Sudi Block	J110	(− 7586.7, 5846.6)	100
	J73	(349.1, − 3178.8)	101		J111	(− 7586.9, 5624.6)	98
	J74	(135.7, − 3327.5)	101		J112	(− 7397.3, 5724.5)	100
	J75	(325.4, − 3324.2)	100		J113	(− 7776.6, 5480.3)	100
	J76	(− 447.9, − 3298.7)	101		J114	(− 7207.8, 5613.5)	98
Suzhou Ningquan United Bridge	J77	(743.8, − 4120.1)	97	Suzhou Guofa & Pingjiang Building	J115	(− 452.2, 2457.8)	99
	J78	(731.4, − 4147.8)	100		J116	(− 427.6, 2516.6)	100
Suzhou Xinsu Wudi Center	J79	(− 404.8, 2840.7)	100	Suzhou Exquisite Bay Garden	J117	(6822.0, 1406.6)	100
	J80	(− 430.4, 2837.4)	100		J118	(6822.0, 1406.6)	100
	J81	(− 456.9, 2839.6)	100		J119	(6822.0, 1406.6)	100
Jiangsu Novavac Biotechnology Co., Ltd. Integrated R&D Building	J82	(− 17,638.8, − 416.0)	54	Da Yangshan Tunnel in Suzhou National Hi-Tech District	J120	(− 15,298.1, 3616.6)	36
	J83	(− 17,745.0, − 439.3)	51		J121	(− 14,289.9, 3274.7)	40
Suzhou Jinchang New Town of China Overseas Building	J84	(− 7089.5, 6715.7)	99	Suzhou Center Square	J122	(5400.2, 629.6)	100
	J85	(− 7241.5, 6272.9)	97		J123	(5495.0, 629.6)	100
	J86	(− 7450.1, 6117.5)	99		J124	(5495.1, 518.6)	100
	J87	(− 7049.0, 6453.8)	98		J125	(5684.9, 74.6)	100
	J88	(− 7243.3, 6308.4)	99		J126	(5400.5, − 36.4)	100
	J89	(− 7318.3, 6126.3)	99		J127	(5590.2, − 36.4)	100
Suzhou Branch Office Buiding of Industrial and Commercial Bank of China	J90	(10,571.6, 798.3)	100	Xiangcheng Section of Suzhou Center Ring Expressway	J128	(− 6238.1, 7340.7)	100
	J91	(10,559.4, 750.6)	100		J129	(− 5462.8, 7648.1)	100
	J92	(10,652.3, 771.7)	100		J130	(− 4992.8, 7634.8)	100
Children's Hospital of Soochow University in Suzhou Industrial Park	J93	(13,064.0, − 352.7)	100	Suzhou Binhe World Trade Center	BH42	(− 5406.5, − 2472.8)	100
	J94	(13,124.7, − 352.7)	100		BH43	(− 5260.4, − 2430.7)	100
	J95	(13,127.7, − 473.7)	70		BH44	(− 4978.7, − 2464.0)	100
	J96	(13,230.0, − 358.3)	94		BH45	(− 4924.6, − 2488.4)	100
Suzhou Industrial Park North Ring Expressway East Extension	J97	(6367.3, 2242.4)	100	No. 2012-G-74(3) Suzhou Sudi Block	BH46	(− 7058.0, 4330.4)	100
	J98	(7463.4, 2183.6)	100		BH47	(− 6970.8, 4230.5)	100
	J99	(7658.2, 2858.5)	100		BH48	(− 6910.2, 4262.6)	100
	J100	(9345.3, 3291.4)	100		BH49	(− 7044.7, 4291.5)	102
	J101	(9345.3, 3291.4)	100		BH50	(− 6962.2, 4345.9)	102
Suzhou Industry Park Moon Bay	J131	(9960.5, − 5675.2)	100	Suzhou Emerald City Phase II and III	DP59	(− 6636.9, − 1296.2)	59
	J132	(10,021.3, − 5695.2)	100		DP60	(− 6757.5, − 1566.0)	100
	J133	(9922.7, − 5815.0)	100		DP61	(− 6676.0, − 1585.9)	97
	J134	(9896.2, − 5918.3)	100		DP62	(− 6579.2, − 1516.0)	98
Suzhou Jiulong Hospital	J135	(10,234.9, 1852.8)	100	Suzhou Parkway International Hotel	DP63	(1465.1, 6792.3)	100
	J136	(10,189.5, 1816.2)	99		DP64	(1426.3, 6714.6)	100
	J137	(10,266.3, 1822.9)	100		DP65	(1359.0, 6774.6)	98

(*continued on next page*)

Table 1 (*continued*)

Source of boreholes	No.	Relative coordinates[b] (X, Y) (m)	Borehole depth (m)	Source of boreholes	No.	Relative coordinates[b] (X, Y) (m)	Borehole depth (m)
Jiangsu Rural Commercial Bank Office Building	J138	(10,274.2, 547.5)	100	Suzhou Science and Technology Town Hospital Project	DP66	(− 20,212.7, 3921.9)	100
	J139	(10,368.1, 513.1)	100		DP67	(− 20,207.2, 3799.8)	100
Suzhou International Nanotechnology Incubation Base Research Building	J140	(14,657.3, − 2444.0)	97	Suzhou Oblique Bridge	DP68	(3360.8, − 6109.2)	100
	J141	(14,738.9, − 2454.0)	100		DP69	(3440.6, − 6306.8)	110
Suzhou Metro Line 3	J142	(− 9093.0, 6505.2)	100	Trolley Line 2 in Suzhou National Hi-Tech District	J169	(− 20,704.1, 3253.7)	100
	J143	(− 8910.6, 4430.3)	100		J170	(− 20,786.3, 4322.6)	100
	J144	(− 8433.3, 2106.8)	97		J171	(− 20,700.8, 4880.9)	100
	J145	(− 8260.3, 277.3)	100		J172	(− 19,752.3, 4754.4)	100
	J146	(− 7492.2, − 170.5)	100		J173	(− 18,423.9, 4458.0)	39
	J147	(− 6864.8, − 947.4)	70		J174	(− 17,211.7, 3817.5)	91
	J148	(− 5916.0, − 2360.6)	100		J175	(− 16,350.2, 4320.4)	40
	J149	(− 4850.9, − 2695.3)	100		J176	(− 15,996.2, 5193.9)	65
	J150	(− 4262.6, − 3953.0)	98		J177	(− 15,793.6, 5714.5)	95
	J151	(− 3990.7, − 4896.1)	80		J178	(− 14,989.1, 6260.6)	74
	J152	(− 3258.0, − 5709.7)	100		J179	(− 14,292.2, 6480.4)	67
	J153	(− 2278.5, − 5773.2)	100		J180	(− 13,650.4, 6609.2)	58
	J154	(− 1520.0, − 5328.4)	100		J181	(− 12,509.2, 6829.0)	97
	J155	(1858.5, − 5239.4)	100		J182	(− 11,995.4, 6932.2)	100
	J156	(3443.5, − 4629.2)	100		J183	(− 11,296.5, 6537.0)	100
	J157	(4348.0, − 3926.4)	100		J184	(− 10,590.9, 6078.6)	100
	J158	(4245.2, − 2794.1)	100		J185	(− 10,045.6, 5410.4)	100
	J159	(5490.9, − 1932.6)	100		J186	(− 9337.3, 5845.5)	100
	J160	(6967.5, − 1980.4)	100		J187	(− 9058.4, 6113.0)	100
	J161	(8360.1, − 1854.9)	100		J188	(− 9487.0, 4816.5)	100
	J162	(11,774.7, − 657.0)	100		J189	(− 9148.8, 4565.7)	100
	J163	(12,136.5, 2334.7)	100	Suzhou Oriental Star	J190	(4964.4, − 158.5)	101
	J164	(13,565.5, 2557.1)	99		J191	(4935.9, − 202.9)	102
	J165	(14,660.4, 4949.7)	97		J192	(4907.5, − 236.2)	100
	J166	(9868.5, − 1957.6)	100	The Second Affiliated Hospital of Soochow University in Suzhou National Hi-Tech District	XP84	(− 10,119.1, 6843.4)	100
	J167	(10,904.0, − 2437.0)	100		XP85	(− 10,040.5, 6814.5)	100
	J168	(11,995.0, − 1994.1)	97		XP86	(− 10,122.1, 6729.1)	100
Pingjiang Branch of the First Affiliated Hospital of Soochow University	XP87	(− 1383.1, 3400.2)	100	Suzhou Rail Transit Line 3 East Section and Line 5 West Section	J227	(− 12,540.7, − 7644.3)	99
	XP88	(− 1242.8, 3434.6)	100		J228	(− 15,908.1, − 9804.4)	71
	XP89	(− 1329.0, 3360.2)	100		J229	(− 14,902.4, − 10,094.1)	86
	XP90	(− 1253.2, 3365.8)	100		J230	(− 13,992.2, − 9434.8)	100
Industrial Park Section of Suzhou Center Ring Expressway	J193	(14,903.5, − 5160.2)	100		J231	(− 12,950.9, − 8584.5)	99
	J194	(13,961.0, 1717.4)	100		J232	(− 12,274.4, − 7946.2)	95
	J195	(14,171.1, − 481.4)	98		J233	(− 11,635.9, − 7205.9)	93
	J196	(14,192.9, − 1940.8)	100		J234	(− 10,924.5, − 6597.6)	29
	J197	(14,194.9, − 2079.9)	100		J235	(− 9218.5, − 5698.5)	100
	J198	(14,193.6, − 3432.7)	100		J236	(− 8348.4, − 5573.1)	100
	J199	(14,273.6, − 3719.2)	100		J237	(− 6837.0, − 5661.9)	100
	J200	(11,220.6, 6988.3)	100		J238	(− 6330.6, − 4508.6)	96
	J201	(13,040.7, 6509.0)	100		J239	(− 5821.7, − 3818.2)	100
	J202	(13,593.9, 3891.8)	100		J240	(− 3850.5, − 3773.8)	100
G&H Blocks in Suzhou Xiangcheng District	J203	(− 1331.4, 6956.6)	100		J241	(− 2988.8, − 2830.3)	100
	J204	(− 1521.0, 6623.6)	98		J242	(− 646.9, − 2584.9)	100
	J205	(− 1426.2, 6734.6)	100		J243	(1522.4, − 2278.6)	97
	J206	(− 1426.2, 6623.6)	99		J244	(2472.8, − 2439.5)	100
	J207	(− 1236.7, 6623.6)	100		J245	(3405.9, − 1879.0)	100
	J208	(− 1426.3, 6401.6)	100		J246	(4226.3, − 1891.2)	100
	J209	(− 1426.3, 6290.6)	100		J247	(5375.6, − 1427.2)	100
	J210	(− 1236.7, 6290.6)	100		J248	(3911.5, − 2032.2)	100
West extension section of Suzhou South Ring Expressway	J211	(− 7858.5, − 6385.6)	94		J249	(5518.2, − 1925.6)	100
	J212	(− 9690.9, − 6559.9)	80		J250	(5635.2, − 802.3)	100
	J213	(− 5592.3, − 5907.2)	95		J251	(5513.7, 1059.2)	100
	J214	(− 6775.7, − 6232.4)	100		J252	(5008.8, 2075.9)	100
Top Future Project of Suzhou Ivick Co., Ltd.	J215	(− 18,187.9, 3379.1)	100		J253	(6089.1, 2975.0)	100
	J216	(− 18,098.6, 3503.4)	97		J254	(6949.8, 3110.5)	100
	J217	(− 17,932.6, 3571.1)	94		J255	(8524.3, 3333.6)	97
	J218	(− 17,828.4, 3480.1)	92		J256	(10,188.2, 4071.7)	100
Suzhou Broadcasting System Modern Media Square Project	J219	(10,879.5, 1113.6)	110		J257	(11,259.1, 4325.9)	100
	J220	(10,934.5, 1086.9)	100		J258	(12,635.7, 4900.9)	100
	J221	(10,762.0, 1024.8)	105		J259	(14,873.7, 5424.8)	98
	J222	(10,751.6, 971.5)	99		J260	(15,963.4, 5594.6)	100
Technology Building 1th and 2th in Suzhou National Hi-Tech District	J223	(− 17,460.0, 1586.4)	90		J261	(15,799.6, 5287.2)	97
	J224	(− 17,514.9, 1649.7)	90	No. 2013-G-87 Suzhou Sudi block	J262	(7251.2, − 7639.9)	100
Suzhou Science and Technology City Standard Factory Building	J225	(− 17,415.7, − 310.6)	52		J263	(7326.1, − 7581.1)	100
	J226	(− 17,520.2, − 376.0)	52		J264	(7373.6, − 7638.8)	100

Table 1 (*continued*)

Source of boreholes	No.	Relative coordinates[b] (X, Y) (m)	Borehole depth (m)	Source of boreholes	No.	Relative coordinates[b] (X, Y) (m)	Borehole depth (m)
Suzhou Rail Transit Line 2 and 4 Control Center	J275	(3102.9, 11,733.0)	92	Suzhou Rail Transit Line 2 and 4 Control Center	J313	(− 2459.0, − 10,673.3)	101
	J276	(2931.2, 11,455.2)	98		J314	(− 3646.9, − 11,530.2)	100
	J277	(974.5, 10,759.0)	100		J315	(− 4503.9, − 12,256.5)	83
	J278	(445.9, 9968.0)	101		J316	(− 5518.4, − 12,572.7)	94
	J279	(343.0, 8580.5)	101		J317	(− 5976.4, − 12,686.9)	77
	J280	(511.5, 6822.2)	100	Trolley Line 1 in Suzhou National Hi-Tech District	J318	(− 20,708.7, 3326.9)	100
	J281	(714.2, 5408.3)	100		J319	(− 19,568.4, 2955.2)	90
	J282	(281.8, 4313.4)	97		J320	(− 19,115.6, 2737.9)	76
	J283	(− 701.3, 3439.1)	98		J321	(− 18,374.5, 2365.6)	82
	J284	(− 494.8, 2655.8)	101		J322	(− 16,951.5, 1635.1)	89
	J285	(− 965.1, 1804.2)	100		J323	(− 16,501.8, 1404.8)	75
	J286	(− 1684.7, 769.2)	100		J324	(− 15,932.4, 1130.2)	58
	J287	(− 1877.8, − 134.9)	101		J325	(− 15,590.1, 982.8)	49
	J288	(− 2150.0, − 1915.0)	100		J326	(− 14,105.4, 637.2)	28
	J289	(− 2147.8, − 2497.6)	99		J327	(− 12,057.3, 305.1)	100
	J290	(− 2154.5, − 3293.6)	100		J328	(− 19,569.9, 2960.6)	77
	J291	(− 1894.9, − 3925.8)	98		J329	(− 9700.1, − 1169.5)	80
	J292	(− 1095.0, − 4664.4)	98		J330	(− 8122.6, − 1021.2)	98
	J293	(− 515.2, − 5305.5)	98		J331	(− 6880.0, − 2078.2)	98
	J294	(− 535.3, − 6430.5)	101		J332	(− 15,020.4, 319.9)	66
	J295	(886.8, − 6843.5)	94		J333	(− 12,052.3, 317.7)	97
	J296	(2497.9, − 7101.1)	100	Suzhou Rainbow Mall	QL25	(1740.0, 6244.0)	100
	J297	(2876.9, − 7177.0)	96		QL26	(1726.8, 6173.0)	100
	J298	(− 3901.1, 9262.9)	100		QL27	(1808.3, 6003.1)	100
	J299	(− 3820.9, 9066.8)	100		QL28	(1788.4, 5911.0)	100
	J300	(− 3220.9, 7087.6)	100		QL29	(1742.9, 5954.3)	100
	J301	(− 2057.5, 5329.1)	100	Changlang South Ring Village Dangerous Building Transformation	BH64	(1350.8, − 3484.0)	100
	J302	(− 1831.6, 4179.1)	90		BH65	(1330.9, − 3560.6)	100
	J303	(− 1655.6, 3208.6)	98		BH66	(1441.9, − 3633.9)	99
	J304	(− 1437.5, 2460.9)	100		BH67	(1307.2, − 3656.1)	100
	J305	(0.0, 0.0)[c]	101		BH68	(1546.3, − 3567.3)	100
	J306	(152.8, − 885.6)	97		BH69	(1099.4, − 3475.2)	100
	J307	(359.3, − 1732.7)	99		BH70	(1224.7, − 3464.1)	100
	J308	(445.5, − 2401.6)	100		BH71	(1174.4, − 3541.8)	100
	J309	(531.8, − 3850.0)	100		BH72	(1127.9, − 3687.2)	100
	J310	(824.0, − 5246.5)	100		BH73	(1104.2, − 3619.5)	100
	J311	(94.0, − 8050.2)	101	Relocation Project of Suzhou Experimental Primary School	BH74	(337.7, − 3441.9)	100
	J312	(− 768.4, − 9362.0)	101				
Suzhou Culture Tourism Square	J400	(− 865.5, 2778.6)	98	Xingming Street Interchange	J414	(3678.9, 1422.2)	100
	J401	(− 816.2, 2851.8)	97		J415	(3262.5, 1899.5)	100
	J402	(− 763.1, 2848.5)	100		J416	(4325.4, 1729.6)	100
Suzhou Guofa Hubing Project	J403	(− 7256.0, − 13,272.0)	82	No. 2014-G-48(1) & (2) Suzhou Sudi Blocks	J417	(− 563.0, − 13,590.6)	99
	J404	(− 7148.7, − 13,257.6)	82		J418	(− 818.5, − 13,694.9)	100
	J405	(− 7162.9, − 13,205.4)	82		J419	(− 499.4, − 13,205.4)	100
Suzhou International Fortune Square	J406	(4950.0, 139.0)	110	Suzhou Canglang New City	BH75	(− 2967.6, − 4821.6)	99
	J407	(4976.6, 120.1)	110		BH76	(− 2901.2, − 4811.6)	100
	J408	(5096.0, 133.4)	100		BH77	(− 2863.2, − 4792.7)	100
Suzhou Zhongnan Center	K1	(9941.6, − 2789.2)	200	North Square Complex Building of Suzhou Railway Station	BH78	(− 849.5, 2115.9)	100
	K2	(10,194.1, − 2911.3)	200		BH79	(− 989.8, 2111.5)	100
Suzhou Suide Technology Golden Mantis Construction Operation Center	J409	(14,288.6, − 4018.0)	100	Suzhou Branch Buiding of Agricultural Bank of China Limited	BH80	(10,710.0, 851.6)	100
	J410	(14,331.3, − 4050.1)	100		BH81	(10,804.8, 851.6)	97
Shanghai-Nanjing Intercity Rail	J411	(17,655.2, 6734.6)	81	Suzhou Emerald City Phase I	BH82	(− 6609.4, − 1359.5)	76
Labor and Personnel Management Center in Suzhou National Hi-Tech District	J412	(− 4762.2, − 2026.6)	91	Suzhou Wuzhong Modern Recreation & Sports Center	BH83	(1264.7, − 5274.5)	100
	J413	(− 4700.6, − 2053.3)	98				

[a] Database was established by Earthquake Administration of Jiangsu Province, China, the authors were not authorized to publish the database.

[b] The setup of the coordinate system is shown in Fig. 1.

[c] Represents the origin of the coordinate system shown in Fig. 1.

2.1. Engineering geology in the urban area of Suzhou

The concerned site (i.e., the urban area of Suzhou and outlined by the broken line in Fig. 1) is covered by the Quaternary deposits of fluvial, lake, lagoon and marine origins. As shown in Fig. 1, the topography at the concerned site is complex. For example, the western portion belongs to the Lake Tai alluvial plain (II3) with interspersed outcrops, consists of the tectonic erosion-induced low hills (I1) and the bottomlands around Lake Tai (I2); whereas, the eastern portion belongs to the lake-swamp plain (II4) and no significant outcrops could be identified. Due to the combined influences of the shore erosions and the alternating deposits of fluvial, lake, lagoon and marine origins, the Quaternary deposits at this site can be regarded as an alternation of clay layer and sand layer; and, the sequence stratigraphic structure of the Quaternary deposits is obvious. The thickness of the Quaternary deposits at the concerned site is relatively large; and, this thickness in the western and southern portions is smaller than that in the eastern and northern portions. The spatial distribution of this thickness can be

attributed to the ancient geomorphology underlain by the Quaternary deposits.

It is worth noting that although four tectonic faults, in terms of the Suxichang fault (F1), Huzhou-Suzhou fault (F2), Kunshan-Jiading fault (F3) and Wujiang-Qiandeng fault (F4), are detected at the concerned site, as illustrated in Fig. 1, these faults can be categorized as the Quaternary faults and the depths of these four faults are relatively large (i.e., larger than 100 m); and, no faults could be identified in the upper 100 m of the Quaternary deposits. Further, almost all engineering activities (e.g., deep excavations, metro tunnels and deep foundations) have been conducted in the upper 100 m of the Quaternary deposits. In such a circumstance, both the spatial characterization of the shear-wave velocity and the 3D characterization of the stratigraphic model, in this paper, would be undertaken in the upper 100 m of the Quaternary deposits in the urban area of Suzhou; and, the stratigraphic model at this site is simplified as a layered geological body.

2.2. Collection of the borehole data in the urban area of Suzhou

It is widely acknowledged that borehole exploration is the most effective method for obtaining the geotechnical and geological information under the ground surface. For example, in situ tests on the undisturbed samples can readily be conducted at various depths at borehole locations, through which the in situ properties could be obtained; meanwhile, the drilling core samples could be collected and then laboratory tests can be performed, through which various soil properties of interest can be obtained. What's more, the sequence stratigraphic structures at borehole locations could be determined based upon a visual inspection of the core samples and the corresponding soil properties. The geotechnical and geological information obtained at borehole locations could help characterize the site information at the concerned site. It can be expected that the effectiveness of the site characterization would be greatly influenced by the size of the borehole data, a larger size of the borehole data would lead to a more effective site characterization. However, the number of boreholes which could be conducted in a given project is oftentimes small due to the limited budget.

Suzhou is one of the most prosperous cities in China. A huge quantity of engineering activities such as deep excavations, metro tunnels and deep foundations have been undertaken in the urban area of Suzhou over the last decades. In order to meet the requirements outlined in the design guidelines provided by the government, a number of borehole explorations were conducted in each and every project. Thus, plenty of borehole explorations were conducted in the urban area of Suzhou. In that the borehole explorations have been carried out by different institutes or companies and the borehole data were owned by various clients, the collection of the borehole data at this site (i.e., the urban area of Suzhou) could be a significant challenge. In this paper, only the borehole data regarding the assessment of the seismic hazards for the engineering site are studied and the corresponding borehole explorations have been conducted by Earthquake Administration of Jiangsu Province, China. Here, a total number of 453 sets of borehole data have been collected in the urban area of Suzhou, among which 397 sets of borehole data are selected and studied in this paper. The spatial distribution of the selected 397 boreholes is illustrated in Fig. 1. The relative coordinates of these 397 boreholes are tabulated in Table 1, in which the setup of the coordinate system is shown in Fig. 1. The number of boreholes located in the eastern lake-swamp plain (II4), western Lake Tai alluvial plain (II3), and tectonic erosion-induced low hills (I1) are 149, 234, and 60, respectively. The borehole investigations lasted about 10 years (i.e., from 2006 to 2015) and the direct cost on the borehole investigations was > 2.0 million US dollars. A short description of the sources of the 397 sets of borehole data is given in Table 1. It can be seen from Table 1 that most of the borehole data were obtained for the construction of the public infrastructures and commercial buildings; and, the depths of most boreholes

studied in this paper are about 100 m, which could allow a complete characterization of the site information in the upper 100 m of the Quaternary deposits in the urban area of Suzhou.

The borehole data analyzed in this paper mainly include the shear-wave velocities and the sequence stratigraphic structures obtained at borehole locations. The shear-wave velocities in the collected borehole database were obtained utilizing the suspension P-S velocity logging method. The adopted suspension P-S logging method uses a probe that contains a source and two receivers spaced 1.0 m apart. This probe is lowered into the drilled borehole to a specified depth where the source generates a pressure wave and the generated wave would be received by the two receivers. The elapsed time between the arrivals of this wave at these two receivers is readily used to calculate the average velocity of this 1-meter-high column of the soil around the borehole. Meanwhile, the drilling core samples at this borehole location could be collected; with the collected core samples, both visual inspections and laboratory tests were undertaken, through which the soil properties of interest could be obtained. The physical and mechanical properties of the core samples can help conduct the soil classification (Ministry of Construction of the People's Republic of China (MCPRC), 2009; Li et al., 2016a; Ganju et al., 2017). From there, the sequence stratigraphic structure at the borehole location can be obtained. In the borehole database established in this paper, the soil classification system outlined in Chinese code GB50021-2001 (MCPRC, 2009) was adopted. Illustrated in Fig. 2 are the shear-wave velocity profiles and the sequence stratigraphic structures obtained at the four borehole locations marked in Fig. 1 (i.e., J332, J53, J419 and J141). In Fig. 2(a), the shear-wave velocities generally increase with the depth. In Fig. 2(b), the Quaternary deposits are consisted of clay layer and sand layer, a short description of the stratum types depicted in Fig. 2(b) is tabulated in Table 2. With the borehole database established, the spatial characterization of the shear-wave velocity and the 3D characterization of the stratigraphic model in the urban area of Suzhou will be conducted in the following text.

3. Spatial characterization of shear-wave velocity along the depth

It is noted that although the time average shear-wave velocity in the upper 30 m at a site, denoted as V_{s30}, is commonly adopted for estimating the site responses and determining the site classes (in earthquake-induced seismic hazards assessment) in current building codes (British Standard Institution (BSI), 2003; Building Seismic Safety Council (BSSC), 2004; Eurocode 8, 2004; Sun et al., 2005; Di Giulio et al., 2008; International Code Council (ICC), 2009; National Earthquake Hazards Reduction Program (NEHRP), 2009; American Society of Civil Engineers (ASCE), 2010; Foulon et al., 2017; Liu et al., 2017), the site responses during an earthquake could also be influenced by the shear-wave velocity at the depth larger than 30 m and this influence could not be ignored (Anderson et al., 1996; Cadet and Duval, 2009; China Earthquake Administration (CEA)., 2015). In most cases, however, only the shear-wave velocity over the shallow depth (e.g., < 30 m) can be available. Thus, the study of the spatial variation of the shear-wave velocity along the depth and the prediction of the shear-wave velocity at the larger depth (e.g., larger than 30 m) are of vital significance. In this section, the spatial characterization of the shear-wave velocity along the depth in the urban area of Suzhou is undertaken: the spatial variation of the shear-wave velocity along the depth is first studied, and then a sequence extrapolation method is proposed for the prediction of the shear-wave velocity along the depth.

3.1. Spatial variation of the shear-wave velocity along the depth

In reference to Fig. 1, the boreholes are mainly located in the eastern lake-swamp plain (II4), western Lake Tai alluvial plain (II3) and tectonic erosion-induced low hills (I1). It is acknowledged that the difference in the topography may lead to the difference in the spatial
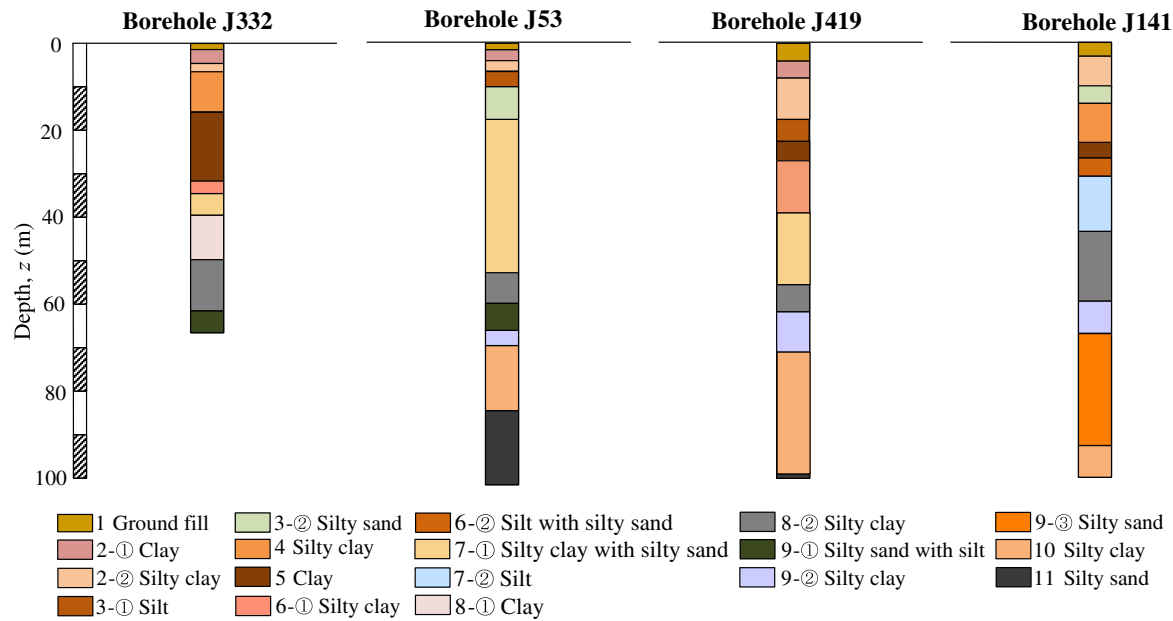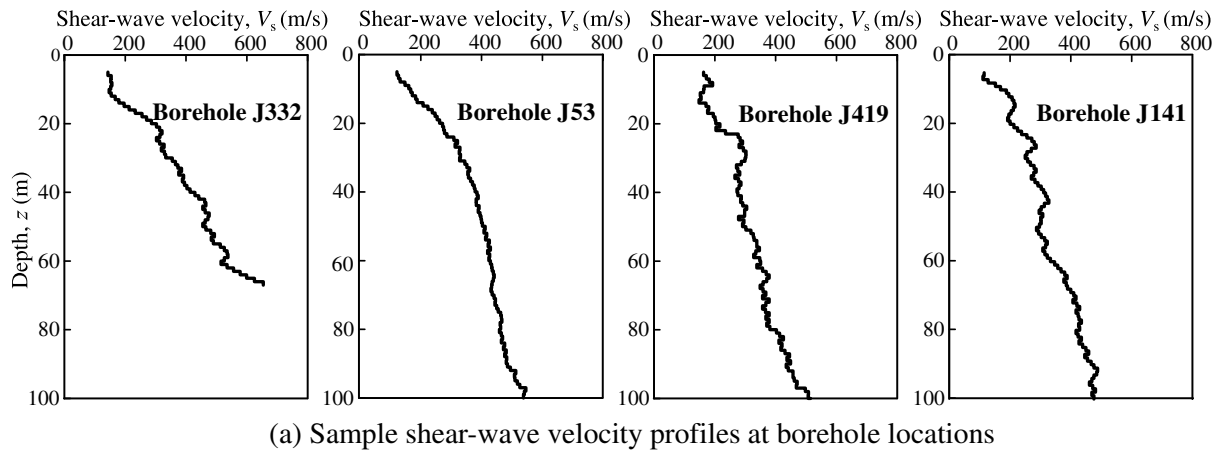
(a) Sample shear-wave velocity profiles at borehole locations

(b) Sample sequence stratigraphic structures at borehole locations

Fig. 2. Sample borehole data collected in the urban area of Suzhou: (a) Sample shear-wave velocity profiles at borehole locations; (b) Sample sequence stratigraphic structures at borehole locations.

variation of the shear-wave velocity along the depth. Thus, the spatial variations of the shear-wave velocity along the depth in the three geological zones are studied separately. Plotted in Fig. 3 are the obtained relationships between the shear-wave velocity, denoted as $V_s(z)$, and the depth (z). Here, $V_s(z)$ represents the shear-wave velocity obtained at depth z and the value is approximated by the time average shear-wave velocity over the depth from $(z - 0.5)$ m to $(z + 0.5)$ m, which could be obtained directly with the suspension P-S velocity logging method.

Fig. 3 depicts that the shear-wave velocity $V_s(z)$ tends to increase with the depth (z). The overall increasing trend of the shear-wave velocity $V_s(z)$ in the eastern lake-swamp plain (II4) and that in the western Lake Tai alluvial plain (II3) are similar; whereas, the relationship between the shear-wave velocity and the depth in the tectonic erosion-induced low hills (I1) is highly scattered. For example, the difference between the maximum shear-wave velocity and the minimum shear-wave velocity (at the same depth) in the eastern lake-swamp plain (II4) and that in the western Lake Tai alluvial plain (II3) are < 100 m/s over the shallow depth (i.e., $z < 15$ m), and the shear-wave velocity difference in the eastern lake-swamp plain (II4) and that in the western

Lake Tai alluvial plain (II3) are < 200 m/s and 300 m/s, respectively, over the large depth (i.e., $z \geq 15$ m). On the other hand, this shear-wave velocity difference in the tectonic erosion-induced low hills (I1) can be as large as 700 m/s. Note that in situations where the depth of the underlying bedrock is smaller, the shear-wave velocity could increase more rapidly with the depth. The scattering of the relationship between the shear-wave velocity and the depth in the tectonic erosion-induced low hills (I1), as shown in Fig. 3(c), might be attributed to the variation of the depth of the bedrock underlain by the Quaternary deposits.

According to Liu et al. (2010) and Wang and Wang (2016), the relationship between the shear-wave velocity $V_s(z)$ and the depth (z) could be captured by linear regression models, quadratic regression models or power regression models, the coefficients of the regression-based models could be estimated using the least square method. In this paper, all these three regression-based models are analyzed; among which, the power regression model is preferred owing to the high coefficient of determination (R^2). The coefficient of determination R^2 of a regression-based model ranges from 0 to 1.0, and a higher coefficient of determination R^2 signals a better fitting of the regression-based

Table 2
Sequence stratigraphic structure in the urban area of Suzhou.

Stratum No.		Soil classification	Characteristics
Soil layer	ID		
1	I	Ground fill	Alluvial deposits; brownish gray, gray and grayish yellow, locally brown, inhomogeneous loose deposit of clayey soils; pewter and grayish yellow, silty clay, soft plastic ~ plastic
2-①	II	Clay	Alluvial-lacustrine or marine, limnetic facies deposits; brown yellow and grayish yellow, plastic ~ hard plastic clay including iron-manganese concretion, locally with slightly dense ~ medium dense silt including mica, grayish yellow
2-②	III	Silty clay	Alluvial-lacustrine or marine, limnetic facies deposits; grayish yellow, gradual transition to gray with depth, soft plastic ~ plastic silty clay including mica and shell fragments, locally with thin layer of silt
3-①	IV	Silt	Coastal deposits; gray and grayish yellow silt with clayey sand, loose ~ slightly dense
3-②	V	Silty sand	Shallow marine deposits; gray and grayish yellow silty sand interbedded commonly with sandy clay, loose ~ slightly dense
4	VI	Silty clay	Alluvial-lacustrine or marine deposits; grayish yellow, yellow gray, pewter, soft plastic, locally plastic, silty clay with reed rhizome, including mica and shell fragments
5	VII	Clay	Alluvial-lacustrine or marine deposits; dark green, grayish yellow, brownish gray, with iron-manganese and calcareous concretion, plastic ~ hard plastic
6-①	VIII	Silty clay	Alluvial-lacustrine or marine deposits; gray, flow plastic ~ soft plastic, with thin layer of silt
6-②	IX	Silt with silty sand	Alluvial-lacustrine or marine deposits; Gray and grayish yellow, silt with silty sand, locally silt with thin layer of silty clay, slightly dense ~ medium dense; including mica and shell fragments
7-①	X	Silty clay with silty sand	Alluvial-lacustrine or marine deposits; gray, ash black, flow plastic silty clay interbedded commonly with medium dense silty sand, locally with silt and lenticular bedding silty sand; including mica and shell fragments
7-②	XI	Silt	Alluvial-lacustrine or marine deposits; gray, medium dense ~ dense
8-①	XII	Clay	Alluvial-lacustrine or marine deposits; dark green, grayish yellow, brownish gray, plastic ~ hard plastic, with iron-manganese and calcareous concretion
8-②	XIII	Silty clay	Alluvial-lacustrine or marine deposits; gray, soft plastic ~ plastic, locally flow plastic, with thin layer of silt and fine sand
9-①	XIV	Silty sand with silt	Alluvial-lacustrine and marine deposits; gray and grayish brown, silty sand interbedded commonly with silty clay
9-②	XV	Silty clay	Alluvial-lacustrine or marine deposits; dark gray silty clay with gravel and sands, sandy clay, plastic ~ hard plastic in upper layer, soft plastic ~ plastic in lower layer
9-③	XVI	Silty sand	Alluvial-lacustrine or marine deposits; gray, grayish brown and dark gray, clayey, silty sand with gravel and sands, locally with sandy clay, dense, including mica and shell fragments
10	XVII	Silty clay	Alluvial-lacustrine or marine deposits; grayish yellow and brown yellow with dark green, gray, silty clay, locally clayey fine sands, plastic ~ hard plastic; including iron-manganese and calcareous concretion, mica and shell fragments
11	XVIII	Silty sand	Alluvial-lacustrine deposits; gray, grayish yellow, and grayish green clayey, silty sands with gravel and sands, dense, occasionally including shell fragments

model. The resulting power regression models together with the coefficients of determination R^2 are illustrated in Fig. 3. The coefficients of determination R^2 derived in the eastern lake-swamp plain (II4), western Lake Tai alluvial plain (II3) and tectonic erosion-induced low hills (I1) are 0.919, 0.882 and 0.619, respectively. These coefficients of determination R^2 indicate that the relationship between the shear-wave velocity $V_s(z)$ and the depth (z) in the eastern lake-swamp plain (II4) and that in the western Lake Tai alluvial plain (II3) are better captured by the power regression model, in comparison to that in the tectonic erosion-induced low hills (I1). Next, both the model predictions and the 95% prediction bands of the shear-wave velocity $V_s(z)$ obtained from these power regression models are plotted in Fig. 3. In Fig. 3(a) and (b), the overall trends of the relationships between the shear-wave velocity

$V_s(z)$ and the depth (z) could be well captured by the model predictions, and most of the measurements (i.e., the shear-wave velocities obtained using the suspension P-S velocity logging method) can be effectively bracketed by the 95% prediction bands; whereas, in Fig. 3(c), the overall trend of the relationship between the shear-wave velocity $V_s(z)$ and the depth (z) could not be captured by the model prediction, and lots of the measurements could not be bracketed by the 95% prediction bands.

In consideration of the poor performance of the power regression model in capturing the relationship between the shear-wave velocity and the depth in the tectonic erosion-induced low hills (I1), as shown in Fig. 3(c), the borehole data of the shear-wave velocity collected in the tectonic erosion-induced low hills (I1) are further divided into three
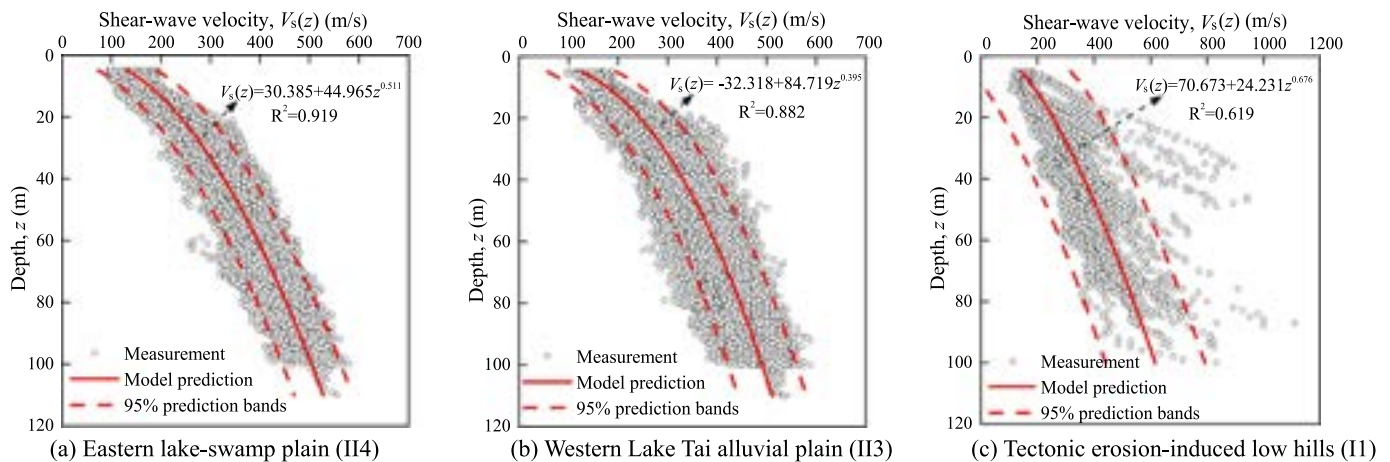

(a) Eastern lake-swamp plain (II4) (b) Western Lake Tai alluvial plain (II3) (c) Tectonic erosion-induced low hills (I1)

Fig. 3. Power regression models of the shear-wave velocity in the urban area of Suzhou: (a) Eastern lake-swamp plain (II4); (b) Western Lake Tai alluvial plain (II3); (c) Tectonic erosion-induced low hills (I1).
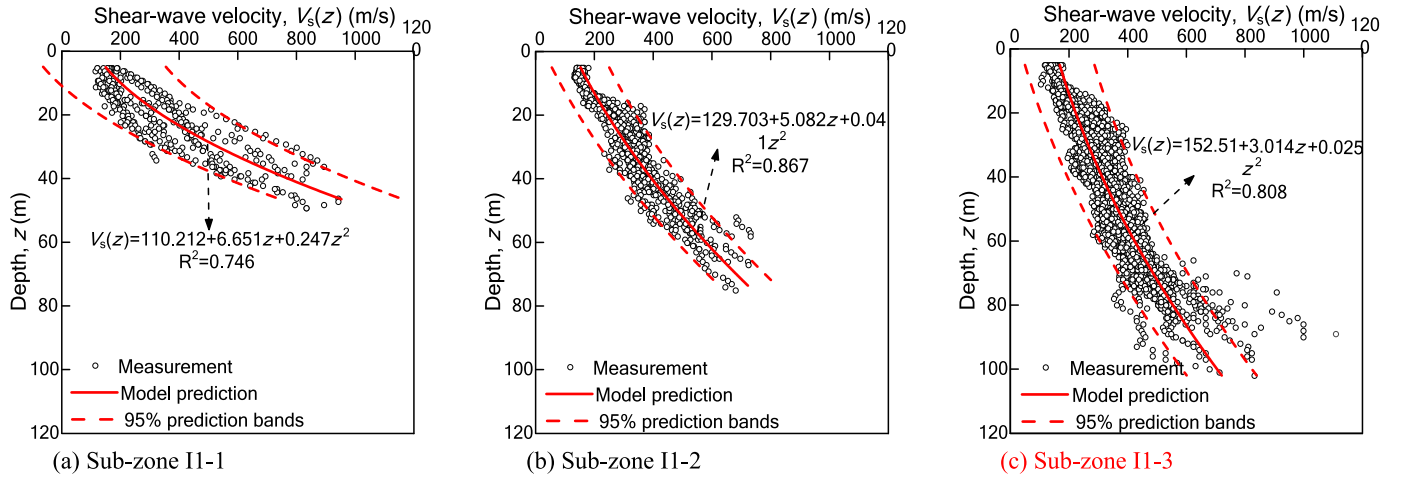
Fig. 4. Quadratic regression models of the shear-wave velocity in tectonic erosion-induced low hills (I1) in the urban area of Suzhou: (a) Sub-zone I1-1; (b) Sub-zone I1-2; (c) Sub-zone I1-3.

sub-zones (i.e., I1-1, I1-2 and I1-3) based upon the depth of the underlying bedrock. The threshold values for the depth of the underlying bedrock between these three sub-zones are 50 m and 75 m. As can be seen in Fig. 4, the relationships between the shear-wave velocity $V_s(z)$ and the depth (z) in these three sub-zones are better captured by the quadratic regression models, in comparison to the power regression model shown in Fig. 3(c). The coefficients of determination R^2 of the quadratic regression models derived in the sub-zones I1-1, I1-2 and I1-3 are 0.746, 0.867 and 0.808, respectively, which are larger than that shown in Fig. 3(c). Further, with the aid of this sub-zone division, the overall trend of the relationship between the shear-wave velocity $V_s(z)$ and the depth (z), in the tectonic erosion-induced low hills (I1), can be better captured by the model prediction and more measurements could be bracketed by the 95% prediction bands, as shown in Fig. 4. From there, it could be concluded that the shear-wave velocity increases with the depth and the relationship between the shear-wave velocity and the depth could be captured by a regression-based model; however, this relationship could be influenced by the topography and the depth of the underlying bedrock.

3.2. Sequence extrapolation method for predicting the shear-wave velocity

It is noted that while the overall trend of the shear-wave velocity $V_s(z)$ with the depth z, in a geological zone, can be captured by the regression-based model shown in Figs. 3 and 4, the relationship between the shear-wave velocity $V_s(z)$ and the depth z at a specified borehole location may not be characterized by this overall trend due to the spatial variation within this geological zone. In such a situation, a sequence extrapolation method is further developed for predicting the shear-wave velocity $V_s(z)$ along the depth (z) at a specified location. It is noted that this sequence extrapolation method stems from the outputs derived in Boore et al. (2011): a linear correlation may exist between the time average shear-wave velocity in the upper 30 m, V_{s30}, and that in the upper depth of H (i.e., $H < 30$ m), denoted as V_{sH}, the degree of linearity of this correlation increases with the depth, and this linear correlation is not degraded by the location. The time average shear-wave velocity in the upper depth of H, V_{sH}, is calculated as follows.

$$V_{sH} = \frac{H}{\int_{z=0}^{z=H} [z/V_s(z)]} \tag{1}$$

On the basis of the borehole data of the shear-wave velocity collected in the urban area of Suzhou, the relationship between the time average shear-wave velocity in the upper depth of ($H + d_H$), $V_{s(H + dH)}$, and that in the upper depth of H, V_{sH}, is readily analyzed, where d_H represents the increment of the depth. Illustrated in Fig. 5 are the

resulting relationships between $V_{s(H + dH)}$ and V_{sH}, in which $H = 10$ m, 20 m, 30 m, 40 m, 50 m, 60 m, 70 m, 80 m, and 90 m and $d_H = 5$ m. Fig. 5 depicts that the relationship between $V_{s(H + dH)}$ and V_{sH} can be well captured by the following linear function.

$$V_{s(H+dH)} = k \cdot V_{sH} \tag{2}$$

where k represents the coefficient of the linear relationship between $V_{s(H + dH)}$ and V_{sH}, which could be estimated with the least square method.

As can be seen in Fig. 5, a linear relationship exists between $V_{s(H + dH)}$ and V_{sH}, and this linear relationship is not degraded by the location (or the geological zone) of the borehole. The observations are consistent with the results obtained in Boore et al. (2011). Meanwhile, as the depth H increases, the coefficient of the linear function k gets closer to 1.0, the coefficient of determination R^2 of the linear function increases and gets closer to 1.0, and the width of the 95% prediction bands of the time average shear-wave velocity $V_{s(H + dH)}$ gets narrower. That is to say, the degree of linearity between $V_{s(H + dH)}$ and V_{sH} increases with the depth H. Further, the relationship between the coefficient of the linear function k and the depth H and that between the coefficient of determination R^2 and the depth H can be obtained, and the results are plotted in Fig. 6. The coefficient of determination R^2 always increase with the depth H, the value is > 0.90 if the depth H is larger than 20 m. The relationship between the coefficient of the linear function k and the depth H could be characterized by the following equation.

$$k = \frac{1.0015H}{-1.8582 + H} \tag{3}$$

With the linear relationships between these time average shear-wave velocities shown in Eq. (2) and Fig. 5, the time average shear-wave velocity in the upper depth of ($H + d_H$), $V_{s(H + dH)}$, could be estimated from that in the upper depth of H, V_{sH}. Here, if the increment of the depth d_H is relatively small (e.g., $d_H = 5$ m adopted in this paper), the shear-wave velocity at the depth of ($H + d_H/2$), denoted as $V_s(H + d_H/2)$, can be approximated from $V_{s(H + dH)}$ and V_{sH}.

$$V_s(H + d_H/2) = \frac{d_H}{\frac{H + d_H}{V_{s(H+dH)}} - \frac{H}{V_{sH}}} \tag{4}$$

Up to now, the sequence extrapolation method is readily developed for predicting the shear-wave velocity $V_s(z)$ along the depth (z). And, the procedures for implementing this sequence extrapolation method are summarized in the following main steps:

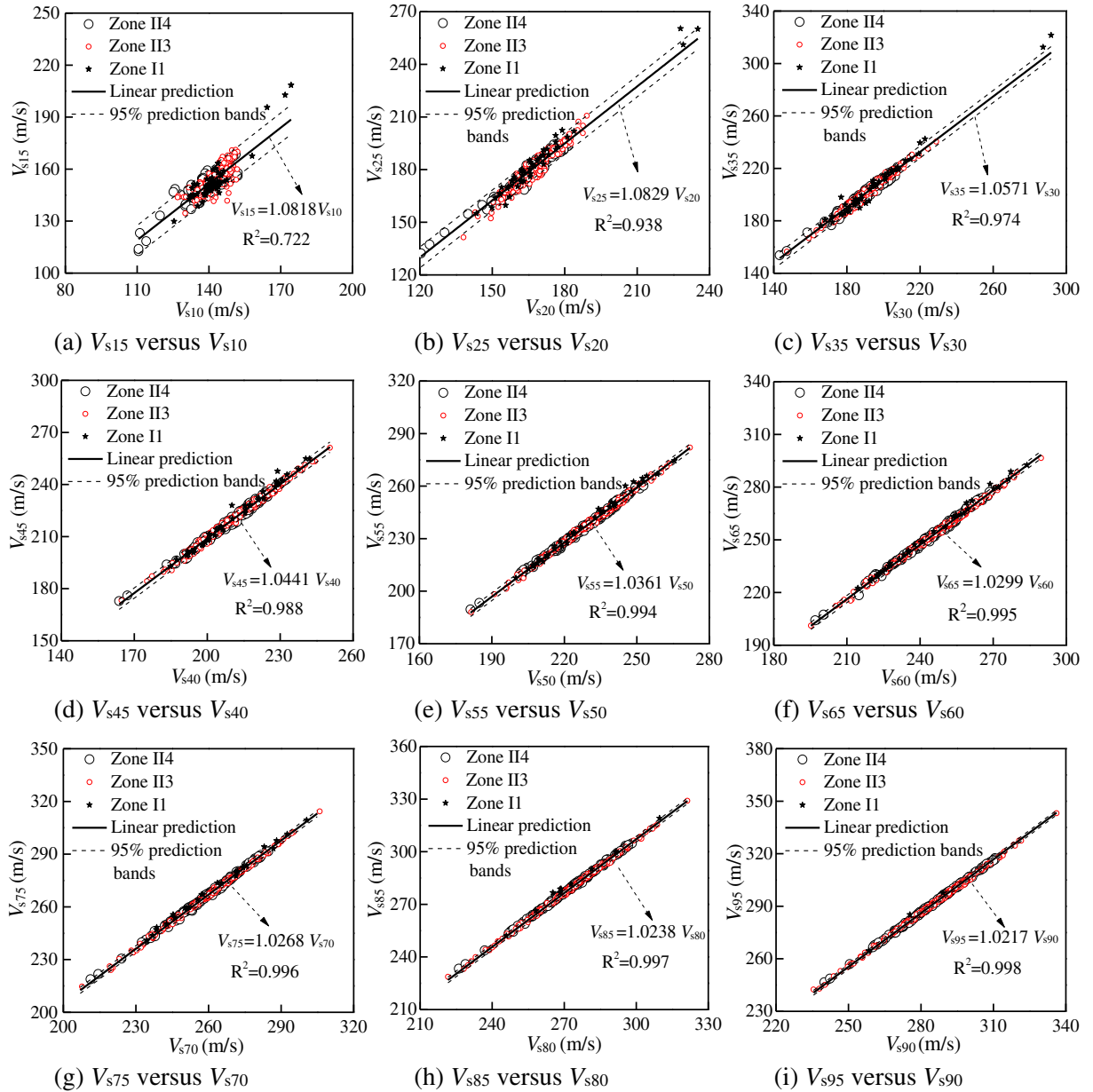Step 1: Derive the relationship between $V_{s(H + dH)}$ and V_{sH} (see

Fig. 5. Linear relationship between the time average shear-wave velocity $V_{s(H+dH)}$ and time average shear-wave velocity V_{sH} in the urban area of Suzhou: (a) V_{s15} versus V_{s10}; (b) V_{s25} versus V_{s20}; (c) V_{s35} versus V_{s30}; (d) V_{s45} versus V_{s40}; (e) V_{s55} versus V_{s50}; (f) V_{s65} versus V_{s60}; (g) V_{s75} versus V_{s70}; (h) V_{s85} versus V_{s80}; (i) V_{s95} versus V_{s90}.
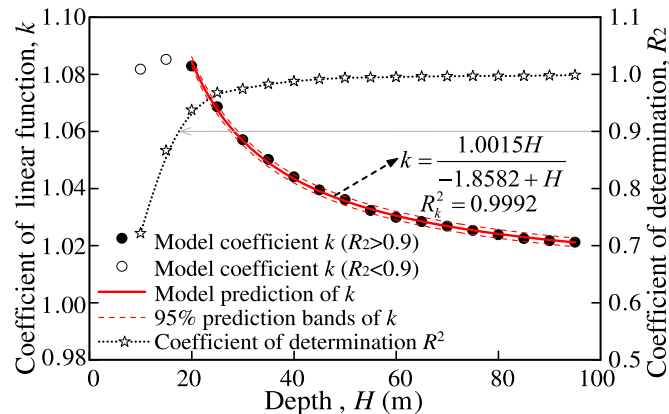

Fig. 6. Relationship between the coefficient of the linear function k in Eq. (2) and the depth H in the urban area of Suzhou.

Fig. 5 and Eq. (2));

Step 2: Predict $V_{s(H+dH)}$ from available V_{sH}, using the relationship obtained in Step 1;

Step 3: Predict $V_s(H + d_H/2)$ from $V_{s(H+dH)}$ and V_{sH}, using the formulation in Eq. (4);

Step 4: Repeat Steps 2–3 until the target depth H is reached.

To validate the sequence extrapolation method developed in this paper, the shear-wave velocity profiles obtained at three representative boreholes (i.e., DP64, XP89 and QL27) are revisited. These three boreholes are located in the eastern lake-swamp plain (II4), western Lake Tai alluvial plain (II3) and tectonic erosion-induced low hills (I1), respectively. In this validation, it is assumed that only the shear-wave velocities in the upper 50 m can be available while those beneath the depth of 50 m need to be predicted. Illustrated in Fig. 7(a) to (c) is the comparison between the shear-wave velocity obtained from the in situ tests and that predicted using the sequence extrapolation method. The prediction of the shear-wave velocity matches the in situ measurement
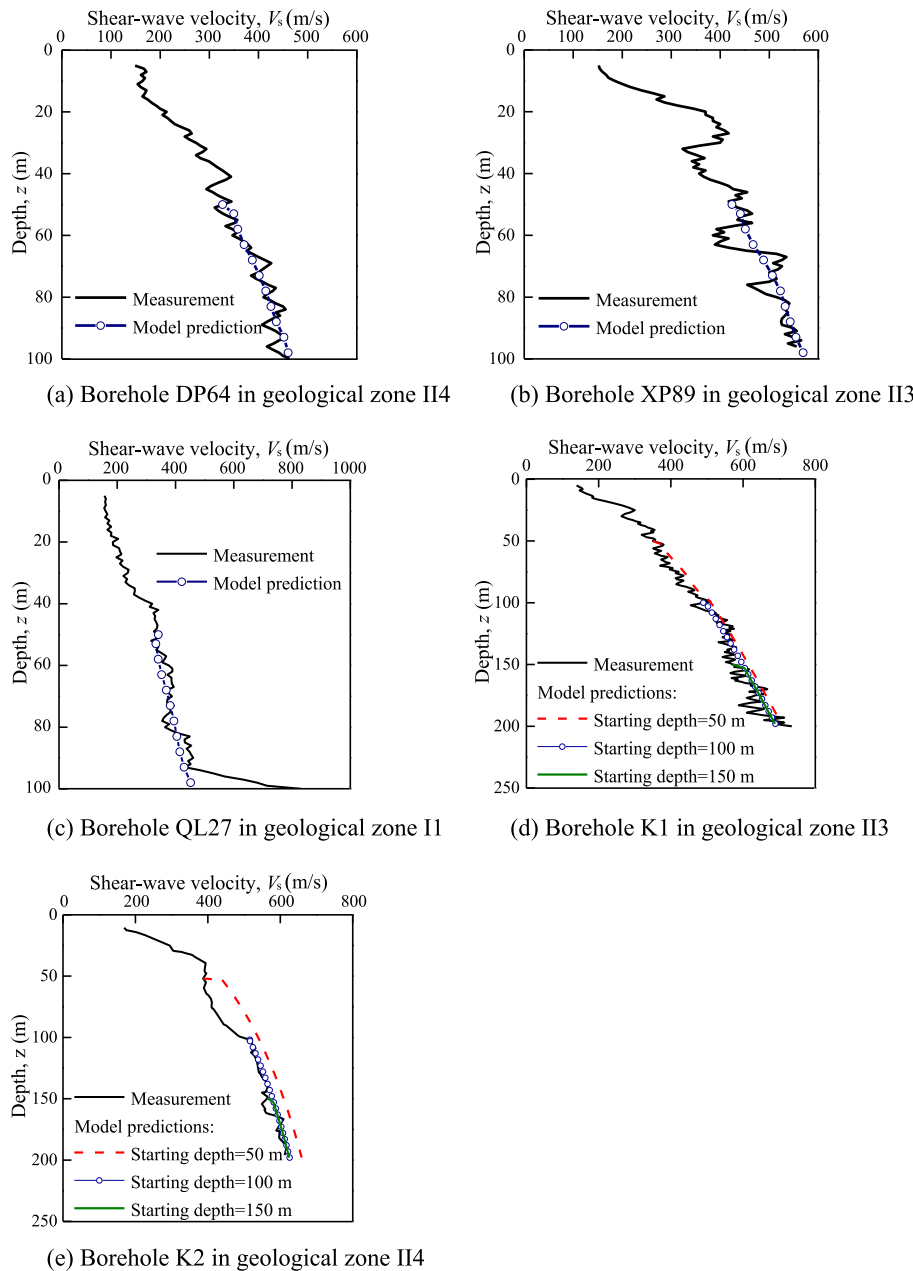
(a) Borehole DP64 in geological zone II4

(b) Borehole XP89 in geological zone II3

(c) Borehole QL27 in geological zone I1

(d) Borehole K1 in geological zone II3

(e) Borehole K2 in geological zone II4

well. Thus, the effectiveness of this sequence extrapolation method is validated. However, if the variation of the shear-wave velocity along the depth was significantly scattered or a sudden change was encountered, the effectiveness of this sequence extrapolation method may be degraded. For example, the shear-wave velocity over the depth of 55 m to 80 m at borehole XP89 and that beneath the depth of 95 m at borehole QL27 could not be captured by the sequence extrapolation method, as illustrated in Fig. 7(b) and (c). Further, the shear-wave velocity profiles at two other deep boreholes (i.e., K1 and K2) are revisited; in which, the sequence extrapolation method could start from the depth of 50 m, 100 m, and 150 m. The comparisons between the measured shear-wave velocity and the predicted shear-wave velocity are illustrated in Fig. 7(d) and (e). The plots in Fig. 7(d) and (e) depict that the performance of this sequence extrapolation method increases with the starting depth; and, the performance of this sequence extrapolation method is degraded in situations where the variation of the shear-wave velocity along the depth beneath the starting depth is not consistent with that at the starting depth. For example, the shear-wave

velocity beneath the depth of 50 m at borehole K2 cannot be captured by the sequence extrapolation method if the starting depth is taken as 50 m, as shown in Fig. 7(e).

4. 3D characterization and visualization of the stratigraphic model in Suzhou

It should be noted that apart from the characterization of the geotechnical parameters along the depth in a geological zone and that at a borehole location, the characterization of the site information, in terms of the geotechnical and geological information, between boreholes is an another significant issue in the site characterization. For example, the characterization of the stratigraphic model at a site is the prerequisite for the analysis, design and construction of the geotechnical system of interest; however, the sequence stratigraphic structure can only be known at borehole locations while that at other positions cannot be known. In this section, the 3D characterization and visualization of the stratigraphic model in the urban area of Suzhou are undertaken: the
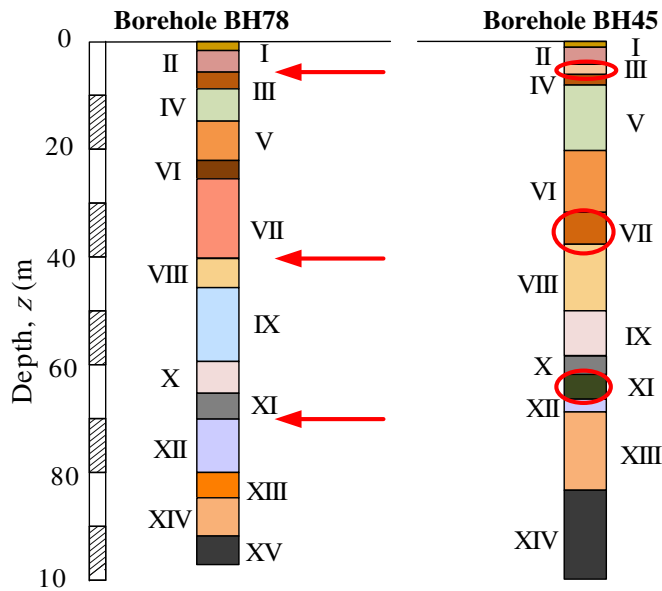
Fig. 8. Illustration of the one-by-one comparison and updating of the sequence stratigraphic structure.

sequence stratigraphic structure at the concerned site is first determined based upon the borehole database established, then the Kriging-based interpolation method is used to characterize the 3D stratigraphic model, finally a 3D visualization of the characterized stratigraphic model is presented.

4.1. Sequence stratigraphic structure in the urban area of Suzhou

Owing to the natural deposit histories, the stratigraphic model at a site is oftentimes a layered structure and the new stratum is usually underlain by the old stratum. The sedimentary sequence of the strata at the site can be represented by the sequence stratigraphic structure. In that the depth and thickness of a stratum could readily be calculated from the elevations of the upper and lower interfaces of this stratum, the sequence stratigraphic structure at an arbitrary position can be characterized by the elevations of the interfaces between adjacent strata. Thus, the characterization of the sequence stratigraphic structure at a site is reduced to the prediction of the elevations of the interfaces between adjacent strata.

Note that a significant step in the characterization of the stratigraphic model at a site is the determination of the sequence stratigraphic structure at the concerned site. In that plenty of borehole explorations have been undertaken in the urban area of Suzhou, the sequence stratigraphic structure at the concerned site could be reasonably captured by the sequence stratigraphic structures obtained at these borehole locations. In the derivation of the sequence stratigraphic structure in the urban area of Suzhou, the sequence stratigraphic structure is assumed to be a continuous sequence, neither stratigraphic break nor strata missing can be permitted. In situations where a stratum is missing, the elevations of the upper and lower interfaces of this missing stratum will coincide with each other and the thickness of this missing stratum will be 0 m. Here, the following procedures are formulated for determining the sequence stratigraphic structure in the urban area of Suzhou:

Step 1: Determine an initial sequence stratigraphic structure based upon the collected borehole data and local experience. For example, the sequence stratigraphic structure obtained at an arbitrary borehole could be taken as the initial sequence stratigraphic structure.
Step 2: Update the initial sequence stratigraphic structure based upon the one-by-one comparison between the initial sequence

stratigraphic structure and the sequence stratigraphic structure obtained at the other borehole.
Step 3: Repeat Step 2 until the one-by-one comparison and updating are undertaken for all the available boreholes. In that the borehole database established in this paper consists of 397 sets of borehole data, the procedures outlined in Step 2 will be repeated 396 times.

To demonstrate the one-by-one comparison and updating of the sequence stratigraphic structure outlined in Step 2, the sequence stratigraphic structure obtained at borehole BH78 is taken herein as the initial sequence stratigraphic structure, which is compared and updated with the sequence stratigraphic structure obtained at borehole BH45, as illustrated in Fig. 8. Here, if the initial sequence stratigraphic structure (i.e., at borehole BH78) is consistent with the sequence stratigraphic structure obtained at the borehole being compared (i.e., at borehole BH45), the initial sequence stratigraphic structure will be reserved; otherwise, new strata will be added into the initial sequence stratigraphic structure and this initial sequence stratigraphic structure will be updated. In the updating of the initial sequence stratigraphic structure, the following criteria should be strictly followed: 1) the order of the strata in the initial sequence stratigraphic structure and that in the sequence stratigraphic structure being compared must be reserved; and 2) the location of the stratum added into the initial sequence stratigraphic structure must be determined such that the strata adjacent to this newly added stratum (in the updated sequence stratigraphic structure) and those in the sequence stratigraphic structure being compared must be consistent. In reference to Fig. 8, stratum III at borehole BH45 will be added to the location between stratum II and stratum III at borehole BH78, stratum VII at borehole BH45 will be added to the location between stratum VII and stratum VIII at borehole BH78, stratum XI at borehole BH45 will be added to the location between stratum XI and stratum XII at borehole BH78. With the borehole database established in Chapter 2, the sequence stratigraphic structure in the urban area of Suzhou could readily be derived using the procedures outlined above (i.e., Step 1 to Step 3), and the result is tabulated in Table 2.

4.2. Kriging-based interpolation method for characterizing the stratigraphic model

Table 2 shows that the sequence stratigraphic structure at the concerned site (i.e., the urban area of Suzhou) consists of 18 strata, in a sequence from the ground fill at the ground surface to the silty sand at the bottom. Thus, the characterization of the stratigraphic model at this site can be reduced to the characterization of the spatial variation of the elevations of the 19 strata interfaces of the 18 strata. Note that although plenty of borehole explorations have been undertaken at the concerned site, the borehole density (i.e., the number of boreholes per unit area) is small in consideration of the huge area at the studied site. And, the elevations of the 19 strata interfaces are only known at borehole locations, whereas those at other positions cannot be known and which have to be predicted from those at borehole locations. In this paper, the existing Kriging-based interpolation method is adopted for the characterization of the spatial variation of the elevations of the 19 strata interfaces from those known at borehole locations. In comparison to other spatial interpolation methods, Kriging-based interpolation method can lead to the best unbiased estimator of the uncertain variables of concern, and can consider the spatial correlations among the uncertain variables; meanwhile, the uncertainty in the prediction of the uncertain variables could be obtained as a byproduct. In that the focus of this chapter is on the deterministic characterization of the stratigraphic model at the concerned site, only the best unbiased estimator of the spatial variation of the elevations of the 19 strata interfaces will be studied in this paper due to the space limitation.

It is widely acknowledged that the stratigraphic model at a given site is deterministic and no uncertainty is involved, and the sequence
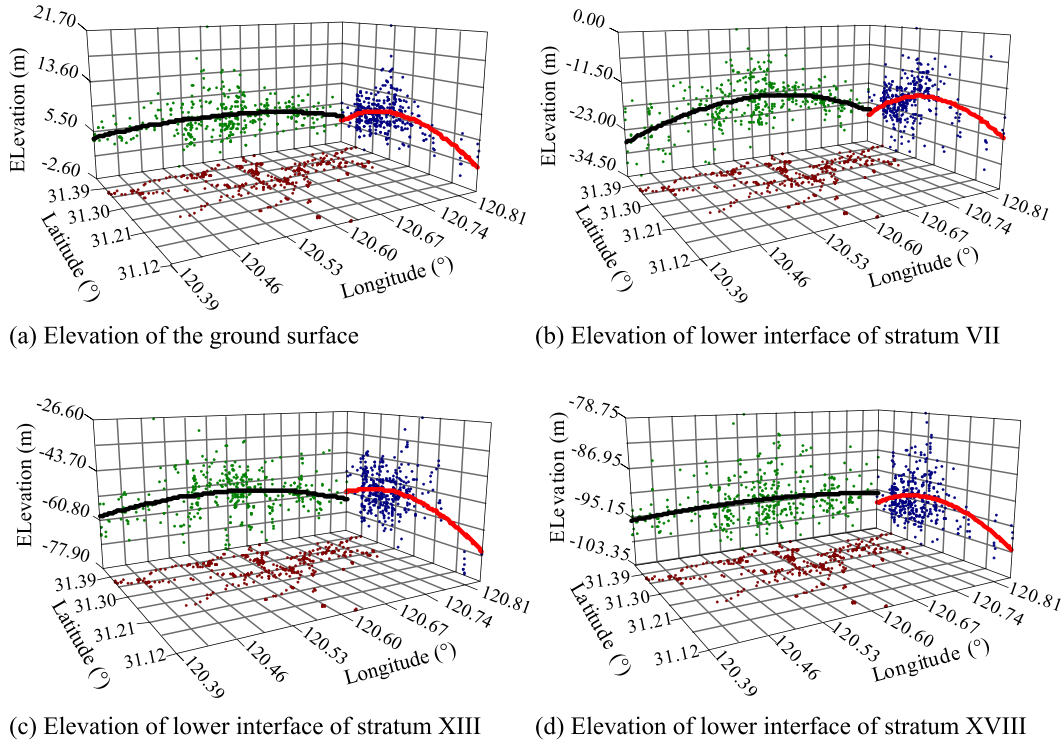
(a) Elevation of the ground surface

(b) Elevation of lower interface of stratum VII

(c) Elevation of lower interface of stratum XIII

(d) Elevation of lower interface of stratum XVIII

Fig. 9. Overall trends of the elevations of the strata interfaces obtained at borehole locations in the urban area of Suzhou: (a) Elevation of the ground surface; (b) Elevation of lower interface of stratum VII; (c) Elevation of lower interface of stratum XIII; (d) Elevation of lower interface of stratum XVIII.

stratigraphic structure at a given position is often correlated to those at nearby positions within this site. However, this stratigraphic model cannot be known to engineers prior to the implementation of borehole explorations. Thus, the stratigraphic model at a site is generally characterized as an uncertain field (Hu and Huang, 2007; Qi et al., 2016). In this paper, the elevations of the 19 strata interfaces are characterized as random fields. For illustration purposes, the stationary Gaussian random field is assumed in this paper and the autocorrelation structure in the horizontal plane is assumed to be isotropic. For example, the elevation of an arbitrary strata interface can be characterized by a stationary random field of $Z(\boldsymbol{D})$, where $\boldsymbol{D} = (x, y)$ represents the position in the horizontal plane at the studied site, x and y represent the coordinate in the west-east direction (or longitude direction) and that in the south-north direction (or latitude direction), respectively. For a stationary random field $Z(\boldsymbol{D})$, the following criteria must be satisfied.

$$E[Z(\boldsymbol{D})] = m \tag{5}$$

$$\gamma(\boldsymbol{D}, \ \boldsymbol{d}) = \gamma(\boldsymbol{d}) \tag{6}$$

where $E(\cdot)$ represents the expected value; m represents a constant which is independent of the position $\boldsymbol{D}$; and, $\gamma(\cdot)$ represents the semivariogram and which is formulated as follows.

$$\gamma(\boldsymbol{D}, \ \boldsymbol{d}) = \frac{1}{2}\mathrm{Var}[Z(\boldsymbol{D}) - Z(\boldsymbol{D} + \boldsymbol{d})] \tag{7}$$

where $\boldsymbol{d}$ represents the distance vector from position $\boldsymbol{D}$ to position ($\boldsymbol{D} + \boldsymbol{d}$), the length of this distance vector $\boldsymbol{d}$ is d. The implication of Eq. (5) is that the expected value of the random field $Z(\boldsymbol{D})$ is independent of the position $\boldsymbol{D}$, and the implication of Eq. (6) is that the autocorrelation of the random field $Z(\boldsymbol{D})$ is independent of the position $\boldsymbol{D}$ and which is only influenced by the separated distance between the two positions of interest. It is noted that although the isotropic stationary Gaussian field is assumed in this study, it is not the limitation of the Kriging-based interpolation method and similar formulations can be set up for the anisotropic, non-stationary, and non-Gaussian field.

With Kriging-based interpolation method, the best unbiased

estimator of the elevation of the strata interface at an arbitrary position, denoted as $\boldsymbol{D^*}$, at the concerned site could be predicted as follows (Li et al., 2016b).

$$Z(\boldsymbol{D^*}) = \sum_{i=1}^{i=n} [\lambda_i(\boldsymbol{D^*}) \cdot Z(\boldsymbol{D_i})] \tag{8}$$

where n represents the number of boreholes implemented at the concerned site; and, $\lambda_i(\boldsymbol{D^*})$ is the weighting factor associated with the elevation $Z(\boldsymbol{D_i})$ observed at borehole position $\boldsymbol{D_i}$. The weighting factor $\lambda_i(\boldsymbol{D^*})$ in Eq. (8) could be solved as follows.

$$\begin{pmatrix} \gamma(\boldsymbol{D_1} - \boldsymbol{D_1}) & \cdots & \gamma(\boldsymbol{D_1} - \boldsymbol{D_n}) & 1 \\ \vdots & \ddots & \vdots & \vdots \\ \gamma(\boldsymbol{D_n} - \boldsymbol{D_1}) & \cdots & \gamma(\boldsymbol{D_n} - \boldsymbol{D_n}) & 1 \\ 1 & \cdots & 1 & 0 \end{pmatrix} \begin{pmatrix} \lambda_1(\boldsymbol{D^*}) \\ \vdots \\ \lambda_n(\boldsymbol{D^*}) \\ \mu \end{pmatrix} = \begin{pmatrix} \gamma(\boldsymbol{D_1} - \boldsymbol{D^*}) \\ \vdots \\ \gamma(\boldsymbol{D_n} - \boldsymbol{D^*}) \\ 1 \end{pmatrix} \tag{9}$$

where μ represents the Lagrangian parameter; $\gamma(\boldsymbol{D_i} - \boldsymbol{D_j})$ represents the semivariogram of the random field of the elevation of the strata interface between position $\boldsymbol{D_i}$ and position $\boldsymbol{D_j}$ ($i, j = 1, 2, \cdots, n$); and, $\gamma(\boldsymbol{D_i} - \boldsymbol{D^*})$ represents the semivariogram of the random field (of the elevation of the strata interface) between position $\boldsymbol{D_i}$ ($i = 1, 2, \cdots, n$) and position $\boldsymbol{D^*}$.

According to the formulation in Eqs. (8)–(9), the best unbiased estimator of the elevation of the strata interface at a specified position is dependent upon the autocorrelation structure of the elevation of the strata interface. However, this autocorrelation structure at a site cannot be known in prior, the determination of which is a great challenge. The autocorrelation structure of the elevation of the strata interface at the concerned site, in this paper, is determined based upon a regression analysis of the collected borehole data. On the basis of the borehole data on the sequence stratigraphic structures known at borehole locations, the data-based or empirical semivariogram $\gamma(d)$ could be estimated.

$$\gamma(d) = \gamma(\boldsymbol{d}) = \frac{1}{2N(\boldsymbol{d})} \sum_{i=1}^{i=N(\boldsymbol{d})} [Z(\boldsymbol{D_i}) - Z(\boldsymbol{D_i} + \boldsymbol{d})]^2 \tag{10}$$

(a) Elevation of the ground surface

(b) Elevation of lower interface of stratum VII

(c) Elevation of lower interface of stratum XIII
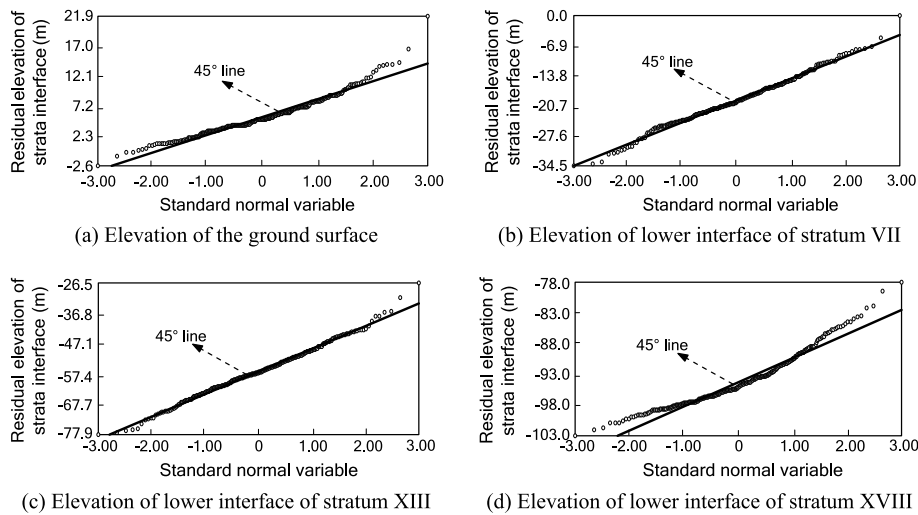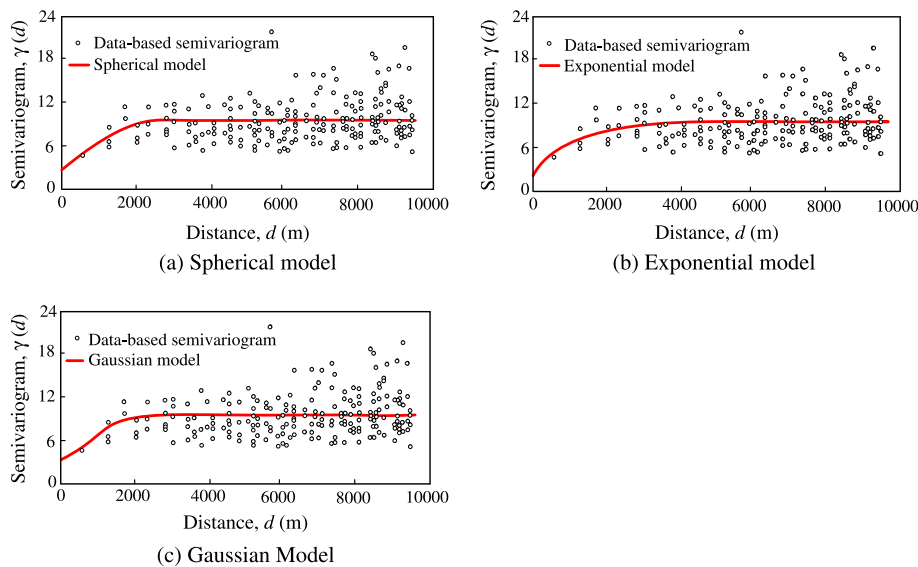

(d) Elevation of lower interface of stratum XVIII

Fig. 10. Validation of the Gaussian random field assumption of the residual elevations of the strata interfaces: (a) Elevation of the ground surface; (b) Elevation of lower interface of stratum VII; (c) Elevation of lower interface of stratum XIII; (d) Elevation of lower interface of stratum XVIII.

(a) Spherical model

(b) Exponential model

(c) Gaussian Model

Fig. 11. Selection of the semivariogram model of the residual elevations of the strata interfaces (i.e., the lower interface of the stratum I – ground fill): (a) Spherical model; (b) Exponential model; (c) Gaussian Model.

where $N(\boldsymbol{d})$ represents the number of pairs of the observed elevations [$Z(\boldsymbol{D})$, $Z(\boldsymbol{D} + \boldsymbol{d})$] that are separated by distance d. From there, the relationship between the data-based semivariogram $\gamma(d)$ and the distance d could be derived, and then the resulting relationship is fitted by a basic semivariogram model. In this paper, spherical model, exponential model and Gaussian model are studied. Note that these three semivariogram models are mostly reported in geotechnical and geological engineering.

4.3. 3D characterization and visualization of the stratigraphic model in Suzhou

It is noted that a prerequisite for the application of the aforementioned Kriging-based interpolation method is that the elevations of the 19 strata interfaces (of the 18 strata shown in Table 2) can be simulated by stationary Gaussian random fields. Thus, the stationary Gaussian random field assumption is validated for the elevations of the 19 strata interfaces. In that the results of the validation are similar among the 19 strata interfaces, only those of the 4 strata interfaces, which are arbitrary selected among the 19 strata interfaces, are presented below. The overall trends of the elevations of the strata interfaces are first studied with the borehole data, and some of the results are plotted in Fig. 9. Fig. 9 depicts that the elevations of the strata interfaces are not

stationary; instead, the elevations of the strata interfaces vary spatially along both longitude and latitude directions. The overall trends of the elevations of the strata interfaces could be attributed to the complex topography, deposit histories, and depths of the underlying bedrock. For example, various geological zones could be identified at this site and different geological zones could exhibit different behaviors of the shear-wave velocity along the depth, as illustrated in Figs. 1, 3 and 4. In such a circumstance, the overall trends of the elevations of the strata interfaces at the concerned site are first derived with a second-order polynomial regression analysis, and then these overall trends are removed from the observed elevations of the strata interfaces. The residual elevations of the strata interfaces could readily be stationary at the concerned site. In that the function of the overall trend depicted in Fig. 9 is site-specific and it also varies with the studied strata interface, the detailed formulation of these trend functions is not listed in this paper due to the space limitation.

Next, the assumption of Gaussian random field of the residual elevations of the strata interfaces are analyzed and some of the results are illustrated in Fig. 10. In Fig. 10, the horizontal axis represents the standard normal variables while the vertical axis represents the residual elevations of the strata interfaces. For each scatter point depicted in Fig. 10, the standard normal variable and the residual elevation of the strata interface could yield the same cumulative distribution function

Table 3
Statistics of the recorded differences of the semivariogram models.

Strata interface	Semivariogram model	Normalized mean of the record difference, μ_{dn}[a]	Standard deviation of the record difference, σ_d[a] (m)
Upper interface of stratum I	Spherical[b]	− 0.005123	2.126221
	Exponential	− 0.010105	2.118169
	Gaussian	− 0.003621	2.172135
Upper interface of stratum II	Spherical	0.000303	2.479335
	Exponential[b]	0.000774	2.461719
	Gaussian	0.000959	2.513402
Upper interface of stratum III	Spherical[b]	− 0.000317	2.559739
	Exponential	− 0.003638	2.503154
	Gaussian	0.001246	2.598760
Upper interface of stratum IV	Spherical	− 0.012986	2.591031
	Exponential	− 0.013139	2.548425
	Gaussian[b]	− 0.007534	2.647642
Upper interface of stratum V	Spherical	− 0.020733	3.316763
	Exponential[b]	− 0.022205	3.267885
	Gaussian	− 0.024368	3.338638
Upper interface of stratum VI	Spherical	− 0.005071	3.042599
	Exponential	− 0.011924	3.015079
	Gaussian[b]	− 0.003072	3.097167
Upper interface of stratum VII	Spherical	0.001393	3.129024
	Exponential[b]	− 0.000121	3.061858
	Gaussian	0.003948	3.172426
Upper interface of stratum VIII	Spherical	0.004962	3.400526
	Exponential[b]	0.006074	3.366166
	Gaussian	0.006877	3.506418
Upper interface of stratum IX	Spherical[b]	− 0.003028	4.007960
	Exponential	0.002216	3.997973
	Gaussian	− 0.005410	4.061347
Upper interface of stratum X	Spherical[b]	− 0.002376	4.921735
	Exponential	0.005369	4.830608
	Gaussian	− 0.008843	5.035839
Upper interface of stratum XI	Spherical[b]	0.000419	5.827263
	Exponential	0.002621	5.740265
	Gaussian	− 0.003556	6.076971
Upper interface of stratum XII	Spherical[b]	0.002866	5.193802
	Exponential	0.006643	5.047794
	Gaussian	− 0.004421	5.517874
Upper interface of stratum XIII	Spherical[b]	0.006890	5.606616
	Exponential	0.010863	5.512907
	Gaussian	− 0.000389	5.981990
Upper interface of stratum XIV	Spherical	− 0.003344	5.227195
	Exponential[b]	0.000662	5.063278
	Gaussian	− 0.002540	5.275775
Upper interface of stratum XV	Spherical	0.011093	5.587638
	Exponential	0.019276	5.425957
	Gaussian[b]	0.008981	5.781706
Upper interface of stratum XVI	Spherical[b]	− 0.000793	5.899924
	Exponential	− 0.007261	5.512335
	Gaussian	− 0.000816	6.382015
Upper interface of stratum XVII	Spherical	0.006610	5.715712
	Exponential	0.006512	5.745755
	Gaussian[b]	0.003736	5.779123
Upper interface of stratum XVIII	Spherical	− 0.002006	4.616764
	Exponential	− 0.005979	4.647815
	Gaussian[b]	0.004709	4.711303
Lower interface of stratum XVIII	Spherical	− 0.017623	2.927866
	Exponential[b]	− 0.013001	2.888510
	Gaussian	− 0.016324	2.944252

[a] $\mu_{dn} = \frac{1}{n_b}\sum_{i=1}^{i=n_b}\frac{D_{bpi} - D_{bi}}{\sigma_{bi}}$, $\sigma_d = \sqrt{\frac{\sum_{i=1}^{i=n_b}(D_{bpi}-D_{bi})^2}{n_b}}$, where n_b is the number of borehole, σ_{bi} is the standard deviation of the residual elevation of the strata interface predicted with the Kriging-based interpolation method at borehole i; and, D_{bpi} and D_{bi} are the residual elevation of the strata interface predicted with the Kriging-based interpolation method and that measured through the borehole exploration.

[b] Represents the best semivariogram model among the three semivariogram model studied.

(CDF). Here, the cumulative distribution functions (CDFs) of the residual elevations of the strata interfaces could be derived with the aid of the cumulative histogram. As can be seen in Fig. 10, the scatter points are distributed along the 45° line, indicating that the residual elevations of the strata interfaces follow Gaussian distributions. As such, the residual elevations of the strata interfaces could be simulated by Gaussian random fields. With the results illustrated in Figs. 9 and 10, the stationary Gaussian random field assumption adopted in this paper is validated.

According to Eq. (10), the relationships between the data-based semivariogram $\gamma(d)$ of the residual elevations of the strata interfaces and the distance d are studied at the concerned site, some of the study results are illustrated in Fig. 11. The empirical relationships shown in Fig. 11 could readily be fitted by the three semivariogram models mentioned above. The fitted semivariogram models could be employed for characterizing the spatial variation of the elevations of the strata interfaces. The plots in Fig. 11 depict that the semivariogram $\gamma(d)$ of the residual elevations of the strata interfaces at this site could be well captured by these three semivariogram models: spherical model, exponential model and Gaussian model. In order to identify the best semivariogram model among these three semivariogram models, the cross-validation, not the coefficient of determination (R^2)-based validation, is conducted here. In the context of this cross-validation, the residual elevations of the strata interfaces at an arbitrary borehole location is first predicted from the those obtained at the left borehole locations, and then the difference between the prediction and measurement (of the residual elevations of the strata interfaces) at this borehole location is recorded; and, this procedure is repeated for all the available borehole locations. Based upon the statistics of the recorded difference of the residual elevations of the strata interfaces (at all 397 boreholes), the best semivariogram model for each and every strata interface can be identified and the results are shown in Table 3. Here, a better model indicates that the normalized mean of the recorded difference is closer to 0 and the standard deviation of the recorded difference is smaller. It must be noted that the construction of an accurate semivariogram usually requires a large number of measurement data pairs with small and equal separated distances, this prerequisite is however not applicable in practice engineering. In Fig. 11, the number of borehole pairs with separated distances < 2000 m is small, and which might lead to the under estimation of the semivariogram; this issue could be avoided with the newly developed Bayesian compressive sampling method (Wang and Zhao, 2017). This limitation of the Kriging-based interpolation method is, however, not discussed in this paper due to the space limitation. Instead, the focus of this chapter is on the application of the Kriging-based interpolation method in the 3D site characterization, not on the discussion of the interpolation methods.

With the results listed above, the aforementioned Kriging-based interpolation method is readily applied to the characterization of the stratigraphic model at the concerned site (i.e., the urban area of Suzhou). The characterization of the stratigraphic model at the concerned site is realized through the following procedures:

Step 1: Discretize the urban area of Suzhou into a set of smaller elements or areas. For example, the size of the smaller elements or areas, in this paper, is automatically determined with the aid of ArcGIS Engine; and, the minimum size is set at 5.0 m by 5.0 m, which is about one-sixth of the minimum distance between adjacent boreholes (i.e., around 30 m).

Step 2: Predict the spatial variation of the residual elevations of the strata interfaces at the concerned site utilizing the Kriging-based interpolation method. The residual elevations of the 19 strata interfaces (of the 18 strata shown in Table 2) within each and every small area at the concerned site are predicted using the best semivariogram model identified in Table 3.

Step 3: Characterize the spatial variation of the elevations of the 19 strata interfaces at the concerned site. The elevations of the 19 strata interfaces are calculated from the residual elevations predicted in Step 2 and the overall trends depicted in Fig. 9.

With the procedures formulated above, the spatial variation of the elevations of the 19 strata interfaces (of the 18 strata) in the urban area of Suzhou could readily be characterized, and some of the results are depicted in Fig. 12. To validate this Kriging-based interpolation method, the sequence stratigraphic structures predicted at three
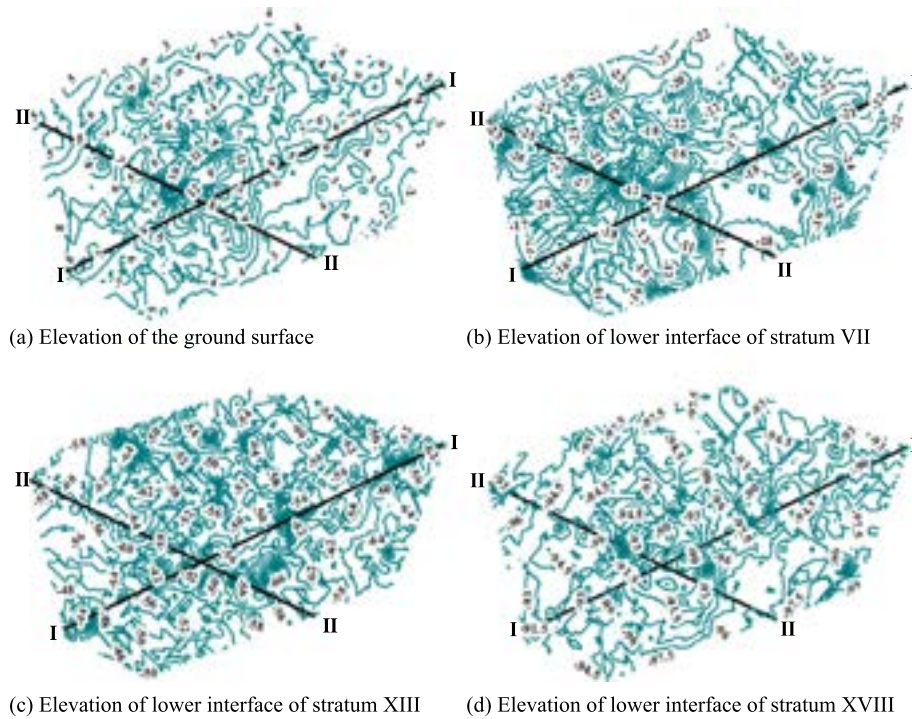
Fig. 12. Spatial variation of the elevations of the strata interfaces in the urban area of Suzhou: (a) Elevation of the ground surface; (b) Elevation of lower interface of stratum VII; (c) Elevation of lower interface of stratum XIII; (d) Elevation of lower interface of stratum XVIII.
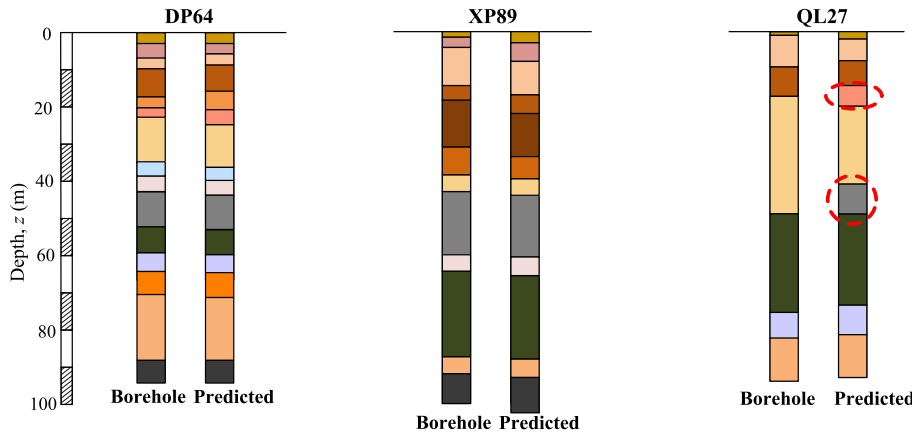
(a) Elevation of the ground surface

(b) Elevation of lower interface of stratum VII

(c) Elevation of lower interface of stratum XIII

(d) Elevation of lower interface of stratum XVIII

Fig. 13. Validation of the Kriging-based interpolation method in predicting the sequence stratigraphic structure.

representative boreholes (i.e., DP64, XP89 and QL27) are illustrated in Fig. 13, also shown in Fig. 13 are the sequence stratigraphic structures obtained from the borehole explorations. It is noted that the sequence stratigraphic structures at borehole DP64 in geological zone II4 and XP89 in geological zone II3 can be satisfactorily predicted using the Kriging-based interpolation method; whereas, two redundant strata are identified in the predicted sequence stratigraphic structure at borehole QL27 in geological zone I1, in comparison to the sequence stratigraphic structure obtained by the borehole exploration. Nevertheless, the overall performance of the adopted Kriging-based interpolation method can be deemed satisfactory. Fig. 14(a) depicts a 3D plot of the spatial variation of the elevations of the 19 strata interfaces (of the 18 strata) in the urban area of Suzhou. For ease of visualization, the predicted elevations of the 19 strata interfaces (of the 18 strata) in the urban area of Suzhou are mapped to ArcGIS Engine, and then a 3D stratigraphic model in the urban area of Suzhou could be obtained, as shown in Fig. 14(b). According to the 3D stratigraphic model shown in Fig. 14(b), the stratigraphic profile in the upper 100 m at the concerned site (i.e., the urban area of Suzhou) could readily be obtained for an arbitrary cross-section. For example, the stratigraphic profiles in the upper 100 m could be obtained for the cross-sections I-I and II-II marked in Fig. 12,

and the resulting stratigraphic profiles are illustrated in Fig. 15.

5. Concluding remarks

This paper presents a three-dimensional (3D) site characterization in the urban area of Suzhou where plenty of borehole explorations have been undertaken. In this paper, a borehole database consists of the borehole data in the urban area of Suzhou is established, then a spatial characterization of the shear-wave velocity along the depth at the concerned site (i.e., the urban area of Suzhou) is presented, and finally a 3D characterization and visualization of the stratigraphic model at the concerned site are presented. The following conclusions are reached based upon the results presented:

(1) The shear-wave velocity, in the urban area of Suzhou, generally increases with the depth, and the overall trend of the relationship between the shear-wave velocity and the depth is captured by regression-based models. However, this relationship could be influenced by the topography and depth of the underlying bedrock. In the urban area of Suzhou, different geological zones are identified and different geological zone exhibits different behavior of the
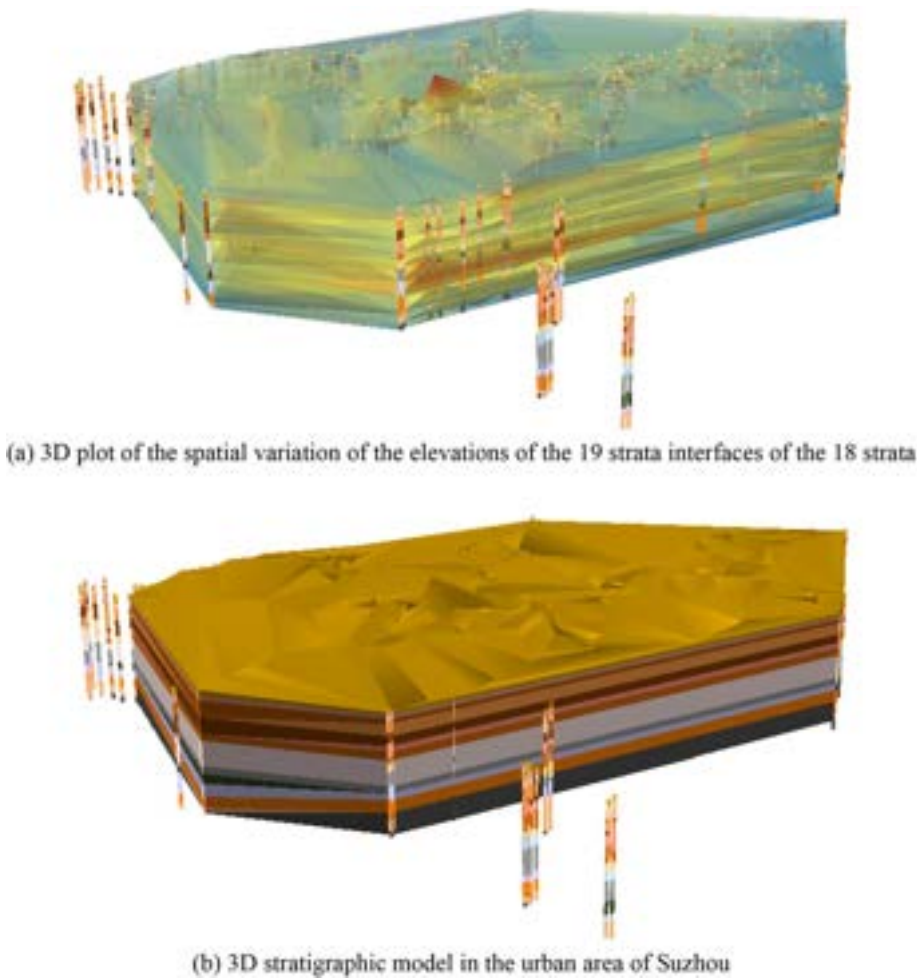
(a) 3D plot of the spatial variation of the elevations of the 19 strata interfaces of the 18 strata

(b) 3D stratigraphic model in the urban area of Suzhou

Fig. 14. 3D visualization of the resulting stratigraphic model in the urban of Suzhou: (a) 3D plot of the spatial variation of the elevations of the 19 strata interfaces of the 18 strata; (b) 3D stratigraphic model in the urban area of Suzhou.
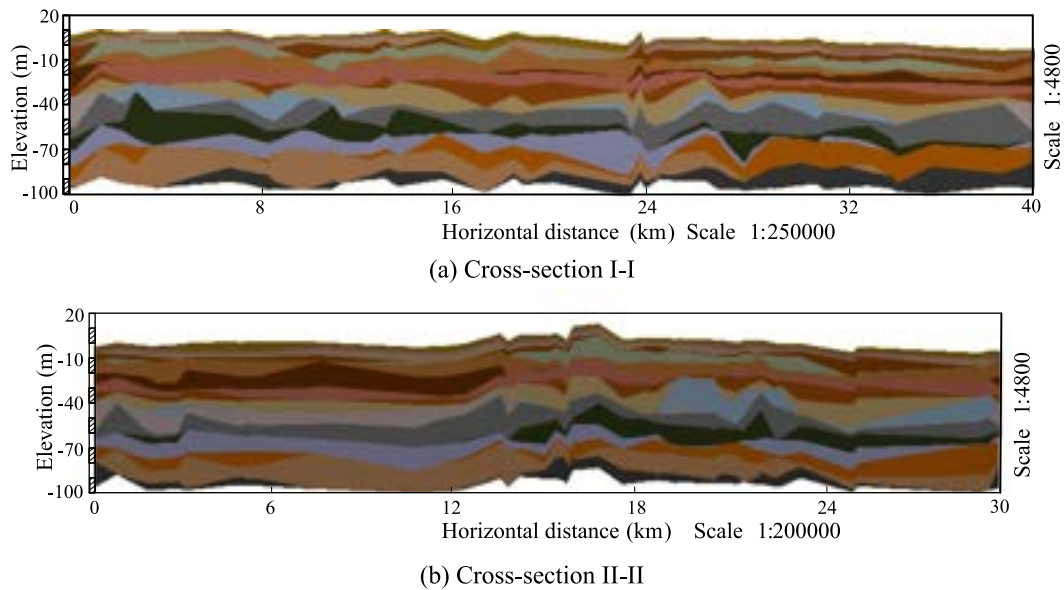

(a) Cross-section I-I

(b) Cross-section II-II

Fig. 15. Schematic stratigraphic profiles of the cross-sections I-I and II-II: (a) Cross-section I-I; (b) Cross-section II-II.

shear-wave velocity along the depth.

(2) A linear relationship exists between the time average shear-wave velocity in the upper depth of $(H + d_H)$ and that in the upper depth of H, the degree of linearity of this relationship increases with the depth. A sequence extrapolation method is, thus, developed for

predicting the shear-wave velocity along the depth. Note that while the effectiveness of this sequence extrapolation method is validated through various applications, the effectiveness of this new method might be degraded in the following scenarios: the shear-wave velocity along the depth is significantly scattered or a sudden change